Contents lists available at ScienceDirect

Comput. Methods Appl. Mech. Engrg.

journal homepage: www.elsevier.com/locate/cma

Adaptive multiscale modeling of polymeric materials with Arlequin coupling and Goals algorithms

Paul T. Bauman, J. Tinsley Oden *, Serge Prudhomme

Institute for Computational Engineering and Sciences, The University of Texas at Austin, 1 University Station C0200, Austin, TX 78712, USA

ARTICLE INFO

Article history:
Received 18 June 2008
Received in revised form 8 October 2008
Accepted 22 October 2008
Available online 30 November 2008

Keywords:
Multiscale modeling
Arlequin coupling
Error estimation
Adaptive modeling
Goals algorithms

ABSTRACT

In this work, the notion of *a posteriori* estimation and control of modeling error is extended to large-scale problems in molecular statics. The approaches developed here involve systematic methods for multiscale modeling in which sequences of hybrid particle–continuum models are generated using an adaptive goal-oriented algorithm designed to control modeling error. We focus on a particular class of problems encountered in semiconductor manufacturing in which a molecular model is used to simulate the deformation of polymeric materials used in the fabrication of semiconductor devices. Algorithms are described which lead to a complex molecular model of polymer materials designed to produce an etch barrier, a critical component in imprint lithography approaches to semiconductor manufacturing. The surrogate model involves a combination of the molecular model of the polymer and a coarse-scale model of the polymer as a nonlinear hyperelastic material. This coupled model is based on the so-called Arlequin method. Coefficients for the nonlinear elastic continuum model are determined using numerical experiments on representative volume elements of the polymer model. Furthermore, a simple model of initial strain is incorporated in the continuum equations to model the inherent shrinking of the material. Three-dimensional numerical results demonstrate the effectiveness of the coupled model, the error estimates, and the adaptive modeling procedure.

1. Introduction

Traditional disciplines of science and engineering are roughly partitioned according to the spatial and temporal scales of particular classes of physical events of interest. The fact that advances in a large and growing number of critical scientific and technological areas require an understanding of events that transcend many scales has highlighted the need for interdisciplinary research and has brought focus on the difficulty of modeling events of multiple scales. As a result, multiscale modeling has become one of the most important and challenging areas of modern computational science.

In recent years, a variety of techniques for multiscale modeling and simulation have been proposed in the literature. Reviews of some of this literature can be found in [18,20,22]. In some respects, multiscale modeling can be viewed as a technique for dimensional reduction, wherein minimal information at the finest scale is used to model events of interest, and coarser scales prevail when they do not influence particular quantities of interest.

Frequently, decisions on what scales are important are made in an ad hoc manner through methods of "coarse-graining", "upscaling", "homogenization", or other techniques. We attempt here to provide a basis for activating the important scales by using *a posteriori* error estimates, based on the relative error between coarse, multiscale models and a base model involving the smallest scale. The error estimates are not necessarily global, but focus on specific quantities of interest. Thus, we follow and extend the methodology of [26,28].

There are four important aspects of the work described here: (1) we attempt to provide a more rigorous basis for selecting the particular scales in a multiscale event that influence the goal of the simulation; (2) we focus on the goal of the simulation: the specific quantity of interest that is the target of the analysis; (3) we implement these methodologies for a difficult and new class of complex engineering problems that could significantly benefit from an accurate multiscale computer simulation: nanomanufacturing of semiconductor devices using imprint lithography; and (4) we extend the methods of error estimation and adaptive control to complex, three-dimensional systems involving molecular models, continuum models, and hybrid models in realistic applications.

The manufacturing of semiconductors, which often hinges upon the ability to understand physical phenomena from the nanoscale to the microscale and beyond, has become one of the most important areas in which multiscale modeling is a critical tool. By 2018, feature sizes of less than 15 nm are expected to be sought for manufacturing of production devices, the current production value

* Corresponding author. Tel.: +1 512 471 3312; fax: +1 512 471 8694.
E-mail addresses: oden@ices.utexas.edu, charlott@ices.utexas.edu (J.T. Oden).

0045-7825/$ - see front matter © 2008 Elsevier B.V. All rights reserved.
doi:10.1016/j.cma.2008.10.014

being 45 nm [29]. It is estimated that, using current techniques, the cost of manufacturing machinery that produce devices with such small features could reach higher than \$50 million [30], a cost generally regarded as prohibitive to the industry. Thus, other processes must be devised to produce the desired technological advancements. Predictive computer simulation could provide an attractive tool to reduce costs in the design of expensive experiments and testing, to assist in obtaining information where experimentation is simply not possible, and to optimize the design of the manufacturing process. Nevertheless, simulations of engineering systems within this context reach beyond the capability of the current computing technologies, making the dimensional reduction for multiscale modeling an essential tool. The development of such simulation tools rests on the edge of contemporary modeling methods and high-performance computing capabilities, and is the focus of this paper.

Here, a molecular model is used to simulate the deformation of polymeric materials used in the fabrication of semiconductor devices. The goal is to develop a surrogate model that incorporates local fine scale information, where needed, and only coarse scale information in the remainder of the material body. This development requires not only the determination of a compatible coarse scale model from the fine scale model, but also the construction of an efficient, stable, and robust method to achieve coupling between the two. Furthermore, the error in local quantities of interest is estimated using the framework of so-called Goal-oriented error estimation. The error estimates can then be used to drive an adaptive *modeling* algorithm where the location and extent of the fine scale model is chosen such that the error in the quantity of interest is within a preset tolerance. These are the *Goals* algorithms [27,28,26].

The remainder of the paper is organized as follows: Following brief descriptions of the theory of Goal-oriented error estimation and the step-and-flash imprint lithography process, Section 2 presents the detailed construction of the molecular base model. Section 3 introduces an algorithm for constructing consistent, continuum models that approximate the coarse-scale behavior of the molecular model. Section 4 develops a new formulation for the coupling of particle and continuum models that is based on using Lagrange multipliers that enforce constraints on a region of overlap between the two models. Section 5 applies the framework for Goal-oriented error estimation established in this section to the surrogates developed in Section 4. Section 6 introduces approximations to the solution of the adjoint problem and evaluation of the residual for more efficient error estimation calculations. Finally, in Section 7, a summary of results and conclusions are discussed.

1.1. Theory of Goal-oriented error estimation

The concept of estimating and controling modeling error in complex models of physical phenomena was advanced in earlier works [25,27,33]. The idea begins with the identification of a base model of the phenomena, characterized by the so-called *primal base problem*,

$$\boxed{\begin{array}{l}\text{Find}\quad \mathbf{u}\in U \text{ such that}\\ B(\mathbf{u};\mathbf{v}) = F(\mathbf{v}) \quad \forall \mathbf{v}\in V\end{array}} \tag{1}$$

where U and V are appropriate topological vector spaces of trial and test vectors, $B(\cdot;\cdot)$ is a semilinear form on $U\times V$, and F is a bounded linear functional on V. The semicolon denotes a possibly nonlinear dependence of $B(\cdot;\cdot)$ on the entry $\mathbf{u}$ to the left of the semicolon, and linear dependence on $\mathbf{v}$.[1]

An example of (1) relevant to the current work is the nonlinear system of algebraic equations characterizing equilibrium configurations of systems of N particles (molecules):

$$E(\mathbf{u}) = \min_{\mathbf{v}\in U} E(\mathbf{v}), \tag{2}$$

where the energy of the system, for every $\mathbf{v}\in U$, assumes the form

$$E(\mathbf{v}) = \sum_{i=1}^{N} E_i(\mathbf{v}) - \sum_{i=1}^{N} \mathbf{f}_i\cdot\mathbf{v}_i. \tag{3}$$

Here, $\mathbf{u} = (\mathbf{u}_1,\mathbf{u}_2,\ldots,\mathbf{u}_N)$ is the N-tuple of displacement vectors of the N molecules relative to a fixed reference configuration, E_i is the energy associated with molecule i, generally determined from inter-molecular energy potentials, $\mathbf{f}_i$ is the prescribed external force applied at site i, and $\mathbf{h}_i$ is a prescribed displacement on $N-N_0$ boundary sites, the displacement vectors $\mathbf{u}_i$ on N_0 molecules being unknowns. The setting is thus one in which the N atoms or molecules making up the model are initially located at points $\mathbf{x}_i$ in a bounded region $\Omega\subset\mathbb{R}^3$ with boundary $\partial\Omega$. The displacements of $N-N_0$ points are prescribed, $\mathbf{u}_i=\mathbf{h}_i$, at points on $\partial\Omega$, while the displacements of the interior N_0 points are unknown, but constitute a minimizer of the total energy that corresponds to an equilibrium configuration of the system. Then, in this case, the forms and spaces in (1) are

$$\begin{aligned}
V &= \{\mathbf{v} = (\mathbf{v}_1,\ldots,\mathbf{v}_N) : \mathbf{v}_i\in\mathbb{R}^3, \mathbf{v}_i = 0, \quad i = N_0+1,\ldots,N\},\\
U &= \{\{\hat{\mathbf{h}}_i\} + V;\ \hat{\mathbf{h}}_i = 0,\ i = 1,\ldots,N_0;\ \hat{\mathbf{h}}_i = \mathbf{h}_i, \quad i = N_0+1,\ldots,N\},\\
B(\mathbf{u};\mathbf{v}) &= \sum_{j=1}^{N_0}\sum_{i=1}^{N_0} \frac{\partial E_i(\mathbf{u})}{\partial \mathbf{u}_j}\cdot\mathbf{v}_j,\\
F(\mathbf{v}) &= \sum_{i=1}^{N_0} \mathbf{f}_i\cdot\mathbf{v}_i.
\end{aligned} \tag{4}$$

The *Goal* of this analysis is not merely the determination of the equilibrium N-vector $\mathbf{u}$ but the determination of a particular functional of $\mathbf{u}$ called the *quantity of interest*, which is characterized by a possibly nonlinear Gâteaux differentiable functional $Q : U\to\mathbb{R}$. The influence of the solution $\mathbf{u}$ on the quantity of interest $Q(\mathbf{u})$ is characterized by an N-vector $\mathbf{p}\in U$ which is a solution of the *adjoint problem*,

$$\boxed{\begin{array}{l}\text{Find}\quad \mathbf{p}\in V \text{ such that}\\ B'(\mathbf{u};\mathbf{v},\mathbf{p}) = Q'(\mathbf{u};\mathbf{v}) \quad \forall \mathbf{v}\in V,\end{array}} \tag{5}$$

where $\mathbf{u}$ is a solution of (1), $\mathbf{p} = (\mathbf{p}_1,\mathbf{p}_2,\ldots,\mathbf{p}_N)$, $\mathbf{p}_i = 0, i > N_0$, and, for $B(\cdot;\cdot)$ in (4),

$$\begin{aligned}
B'(\mathbf{u};\mathbf{v},\mathbf{w}) &= \lim_{\theta\to 0}\theta^{-1}[B(\mathbf{u}+\theta\mathbf{w};\mathbf{v}) - B(\mathbf{u};\mathbf{v})],\\
Q'(\mathbf{u};\mathbf{v}) &= \lim_{\theta\to 0}\theta^{-1}[Q(\mathbf{u}+\theta\mathbf{v}) - Q(\mathbf{v})],
\end{aligned} \tag{6}$$

and, in the case that $(4)_3$ holds

$$B'(\mathbf{u};\mathbf{v},\mathbf{p}) = \sum_{k=1}^{N_0}\sum_{j=1}^{N_0}\sum_{i=1}^{N_0} \mathbf{v}_j\cdot\frac{\partial^2 E_i(\mathbf{u})}{\partial\mathbf{u}_j\partial\mathbf{u}_k}\cdot\mathbf{p}_k. \tag{7}$$

Note that the adjoint problem (5) is linear in $\mathbf{p}$.

1.2. Surrogate models and errors in quantities of interest

Let $(\mathbf{u}_0,\mathbf{p}_0)$ be an *arbitrary* pair of N-vectors in $U\times V$. Then, it is shown in [25] (see also [26]) that the error in the quantity of interest Q obtained by evaluating Q at $\mathbf{u}_0$ instead of at a solution $\mathbf{u}$ of (1) is

[1] Eq. (1) is obviously equivalent to the abstract problem $A\mathbf{u} = F$ in V', where A is an operator mapping U into the dual V' of V and $B(\mathbf{u};\mathbf{v}) - F(\mathbf{v}) = \langle A\mathbf{u} - F, \mathbf{v}\rangle$ for every $\mathbf{v}$ in V.

$$\boxed{\begin{aligned}\mathscr{E} &= Q(\mathbf{u}) - Q(\mathbf{u}_0) = \mathscr{R}(\mathbf{u}_0;\mathbf{p}) + \varDelta\\ &= \mathscr{R}(\mathbf{u}_0;\mathbf{p}_0) + \mathscr{R}(\mathbf{u}_0;\mathbf{p}-\mathbf{p}_0) + \varDelta,\end{aligned}} \tag{8}$$

where $\mathscr{R}(\cdot;\cdot)$ is the residual functional,

$$\mathscr{R}(\mathbf{u}_0;\mathbf{v}) = F(\mathbf{v}) - B(\mathbf{u}_0;\mathbf{v}), \quad \mathbf{v} \in V, \tag{9}$$

and $\varDelta$ is a remainder functional of higher order in the errors $\mathbf{e}_0 = \mathbf{u} - \mathbf{u}_0$ and $\varepsilon_0 = \mathbf{p} - \mathbf{p}_0$. Clearly, $\mathscr{R}(\mathbf{u}_0;\mathbf{v})$ is linear in the test vector $\mathbf{v}$. The derivation of (8) assumes that the forms $B(\cdot;\cdot)$ and $Q(\cdot)$ are thrice differentiable in the sense of (6). The remainder $\varDelta$ is then of the form

$$\begin{aligned}\varDelta = {}&\frac{1}{2}\int_0^1 B''(\mathbf{u}_0 + s\mathbf{e}_0;\mathbf{e}_0,\mathbf{e}_0,\mathbf{p}_0 + s\varepsilon_0) - Q''(\mathbf{u}_0 + s\mathbf{e}_0;\mathbf{e}_0,\mathbf{e}_0)ds\\ &+\frac{1}{2}\int_0^1 (Q'''(\mathbf{u}_0 + s\mathbf{e}_0;\mathbf{e}_0,\mathbf{e}_0,\mathbf{e}_0) - 3B''(\mathbf{u}_0 + s\mathbf{e}_0;\mathbf{e}_0,\mathbf{e}_0,\varepsilon_0)\\ &- B'''(\mathbf{u}_0 + s\mathbf{e}_0;\mathbf{e}_0,\mathbf{e}_0,\mathbf{e}_0,\mathbf{p}_0 + s\varepsilon_0)) \times (s-1)sds.\end{aligned} \tag{10}$$

See [25].

The main ideas behind this approach to multi-scale modeling and estimating and controlling modeling error developed in this investigation are

(i) Choose $(\mathbf{u}_0, \mathbf{p}_0)$ "close" to the solution pair $(\mathbf{u}, \mathbf{p})$ so that the remainder $\varDelta$ is negligible compared to $\mathscr{R}(\mathbf{u}_0;\mathbf{p})$.

(ii) A pair $(\mathbf{u}_0, \mathbf{p}_0)$ "close" to $(\mathbf{u}, \mathbf{p})$ can presumably be the solution of *surrogate* primal and adjoint problems of size $M \ll N$ possibly corresponding to models of the event involving much larger (coarser) scales; e.g.

$$\boxed{\begin{aligned}&(\mathbf{u}_0, \mathbf{p}_0) \in U_0 \times V_0:\\ &B_0(\mathbf{u}_0;\mathbf{v}) = F_0(\mathbf{v}) \quad \forall \mathbf{v} \in V,\\ &B_0'(\mathbf{u}_0;\mathbf{v},\mathbf{p}) = Q'(\mathbf{u}_0;\mathbf{v}) \quad \forall \mathbf{v} \in V,\end{aligned}} \tag{11}$$

where U_0 and V_0 are the spaces corresponding to the coarser scale model. Note that $(\mathbf{u}_0, \mathbf{p}_0)$ must be mapped to $U \times V$ to evaluate the residual in this case.

(iii) Generate a sequence of surrogate problems with solutions $(\mathbf{u}_0^k, \mathbf{p}_0^k)_{k\geqslant 1}$, so that for some integer m_0, the modeling error satisfies

$$|Q(\mathbf{u}) - Q(\mathbf{u}_0^k)| \approx |\mathscr{R}(\mathbf{u}_0^k, \mathbf{p}_0^k) + \mathscr{R}(\mathbf{u}_0^k, \mathbf{p} - \mathbf{p}_0^k)| \leqslant \gamma_{\text{tol}}, \quad k > m_0, \tag{12}$$

where γ_{tol} is a preset error tolerance.

The implementation of these general ideas, of course, can present major challenges. To wit

(i) The generation of appropriate sequences of surrogates is the fundamental problem of multi-scale modeling. Surrogates can be based on coupling particle and continuum models, such as is the case in so-called atomistic-to-continuum approaches, or by dimensional reduction approaches such as methods based on the quasi-continuum methodologies [24].

(ii) The calculation of the solution $\mathbf{p}$ of the base adjoint problem, in general, represents an enormous and complex algebraic problem, even though it is linear. To avoid such calculations, one hopes to generate a sequence of surrogate adjoint solutions $\mathbf{p}_0^k$ that converges rapidly to $\mathbf{p}$ in V.

(iii) The modeling error estimate, $\mathscr{E} \approx \mathscr{R}(\mathbf{u}_0;\mathbf{p})$, involves the repeated evaluation of the full residual $\mathscr{R}(\mathbf{u}_0;\mathbf{p})$ at pairs $(\mathbf{u}_0^k, \mathbf{p}_0^k)$ of surrogate solutions. Approximations $\mathscr{R}^k(\cdot;\cdot)$ of the residual may be generated to reduce the cost of these calculations.

One major thrust of this work is the construction and implementation of such an algorithm and the characterization of its accuracy and efficiency.

1.3. Step and flash imprint lithography

The principal application area of the multiscale modeling methods developed in this work involves modeling and simulation of molecular models of a manufacturing process called *step and flash imprint lithography* (SFIL) [2]. The primary goal is to imprint features of a computer chip, such as wires, into a metal substrate. Imprint lithography proposes to use mechanical processes at room temperature to physically imprint the desired features and has already demonstrated capabilities of producing 32 nm features. Typical manufacturing units cost approximately $5 million dollars [17], a substantial savings over the predicted optical lithography costs.

A typical configuration used in imprint lithography consists of the following:

- *The imprinting template*: The template is made of quartz crystal and has the desired features etched onto its lower surface through an electron beam etching procedure. On the imprinted surface of the template is a release layer designed to allow the template to be easily removed from the polymerized etch barrier. The release layer is a perfluro alkane, very similar to Teflon.
- *The etch barrier solution*: The etch barrier undergoes chemical reactions when subjected to ultra-violet light. These chemical reactions form a polymer through a process called polymerization.
- *The transfer layer*: The transfer layer is a glassy styrene type of polymer used to "add aspect ratio" to the features imprinted in the etch barrier. In other words, the transfer layer increases the height-to-width ratio of the features to enhance the fidelity of the crucial, final etching procedures.
- *The substrate layer*: The substrate layer is generally made of silicon. Imprinting the desired features into the substrate is the primary goal of the lithography process.

The process of imprint lithography can be decomposed into eight stages [19]:

(i) The liquid etch barrier solution is deposited in drops onto the transfer layer at several locations.

(ii) The template is placed on the surface so that the etch barrier solution fills the etched features on the template.

(iii) The sample is illuminated with ultra-violet light for approximately 30 s initiating the polymerization process thereby "solidifying" the features in the etch barrier.

(iv) The template is removed leaving the relief pattern.

(v) An etch is performed to break through the residual etch barrier solution between the features. This is the so-called breakthrough etch.

(vi) Another etch is performed, but now the goal is to etch the transfer layer so that the relief pattern is the same as the etch barrier, but the features have much larger aspect ratios.

(vii) A final etch is performed to etch the feature pattern into the substrate.

(viii) Finally, the substrate is submerged in an organic solvent in order to remove residual polymeric materials from the substrate.

Fig. 1 illustrates the entire process schematically. The key to success of this process is the fidelity of the features in the etch barrier prior to the breakthrough etch. The reactive ion etch that is

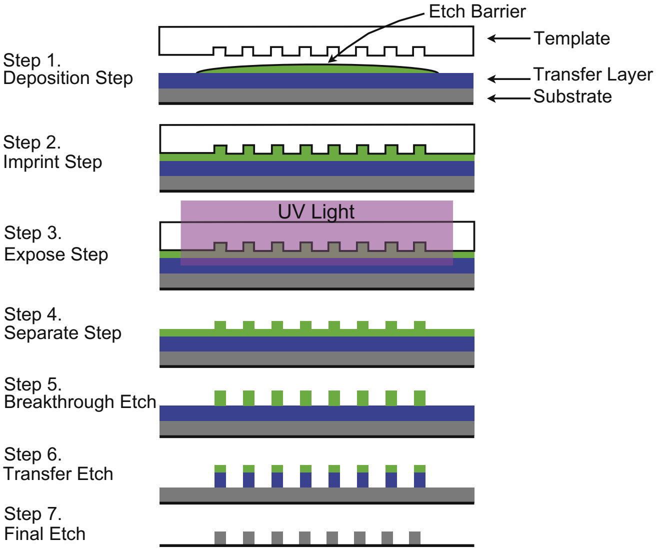

Fig. 1. The step and flash imprint lithography (SFIL) process.

used requires sharp features in order to produce a relief that mimics the template pattern.

2. The polymerization process and the polymer model

We now investigate a significant computational problem often overlooked in the literature on computational modeling: the development of the base computational model itself. In the SFIL process, described in Section 1.3, the target etch barrier material is produced in two steps

(i) A solution of chemical constituents flows into the template relief (the template contours) as the template is pressed toward the transfer layer.
(ii) Ultra-violet (UV) light is passed through the template (which is translucent quartz) into the mixture.

The application of ultraviolet light causes chemical reactions between the chemical constituents which leads to the formation of chain-like macromolecules consisting of various repeated molecular units. The units are monomers and the macromolecules are polymer chains. This chemical process is referred to as *polymerization*. The details on the materials as well as the chemical reactions for a representative acrylate mixture are given in [23,13,6], for example.

2.1. A kinetic Monte-Carlo process

The equations of chemical kinetics only provide the global species concentrations as functions of time (and the initial species distributions). To determine the molecular structure at the termination of the polymerization process, one must follow the likely chemical reactions that can occur between the molecular components. The possible conformations resulting from reactions of a given initial distribution of constituents can be generated through a Monte-Carlo-like algorithm that shall be referred to here as the kinetic Monte-Carlo process. This process was introduced in [13] and is discussed here for completeness. The key to simulating the polymerization process in this way is to observe that the rate coefficients from chemical kinetics for each reaction is related to the classical Arrhenius law. Within this context, the Arrhenius law provides the probability of reaction occurrence:

$$P = Ce^{-E_a/\kappa T} \propto k, \tag{13}$$

where E_a is the activation energy and k is the reaction rate constant.

We introduce a three-dimensional regular lattice $\mathscr{L}$ where the number of lattice sites is set equal to the estimated number of constituent molecules in a cube Ω of the initial etch barrier mixture. There are five constituents in the SFIL process under study: the monomer M_1, the monomer M_2, the cross-linker XL, the initiator I, and possible voids V. The voids are introduced to allow diffusion of the constituents during the model process. Let the concentrations by volume of each of these constituents before photo-curing (UV exposure) be denoted by C_{M_1}, C_{M_2}, C_{XL}, C_I, and C_V, respectively. Then

$$C_{M_1} + C_{M_2} + C_{XL} + C_I + C_V = 1.0. \tag{14}$$

Five disjoint subintervals of $I = [0, 1]$ are defined with length equal to the fraction of each constituent:

$$\begin{aligned}
&I_{M_1} = [0, C_{M_1}],\\
&I_{M_2} = [C_{M_1}, C_{M_1} + C_{M_2}],\\
&I_{XL} = [C_{M_1} + C_{M_2}, C_{M_1} + C_{M_2} + C_{XL}],\\
&I_I = [C_{M_1} + C_{M_2} + C_{XL}, C_{M_1} + C_{M_2} + C_{XL} + C_I],\\
&I_V = [1 - C_V, 1].
\end{aligned}$$

Let N denote the number of cells in $\mathscr{L}$ and let j be an index which specifies the constituent types $j = \{M_1, M_2, XL, I, V\}$. Then a molecular constituent is assigned to each cell as follows.

(i) Boundary cells are assigned either a template molecule or a transfer layer molecule, depending on the location of the part of the boundary where the cell is located.
(ii) Each lattice site is visited in order and a uniform random number, r, is selected such that $0 \leqslant r \leqslant 1$. If $r \in I_j$, then the cell is assigned constituent j.
(iii) A random swapping procedure of the cells is used to further "randomize" the lattice.

Fig. 2 illustrates the lattice placement process schematically.

The following Monte-Carlo type algorithm describes the polymerization of the now populated lattice [13]. Let N_c be the number of cycles, N_{c_i} be the number of iterations per cycle, and N_i the number of initiation cycles. Then, for each cycle C, an *initialization* loop and a *propagation* loop is executed.

(i) Initialization loop
  (a) Select a random lattice site and check if the constituent randomly assigned to the cell is an initiator.
  (b) If the site is an initiator, select a uniform random number r, $0 \leqslant r \leqslant 1$. If $r \leqslant P_I$, P_I being the probability of an initiator reacting, the initiator reacts and the cell is now labeled a free radical R; otherwise the initiator does not react and the cell label is unchanged.
  (c) Repeat N_i times.

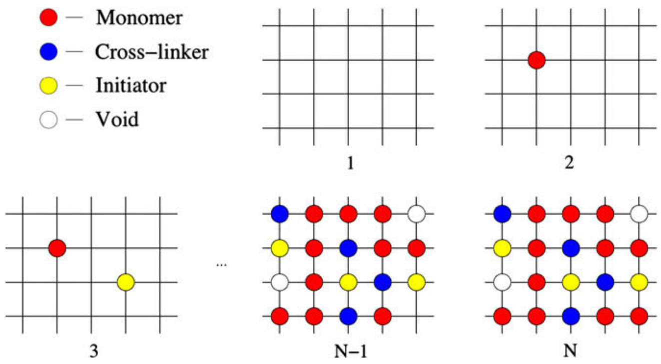

Fig. 2. A schematic of the lattice cell placement algorithm.

(ii) Propagation loop
  (a) A random site is selected and the cell label j identified.
  (b) If j is a void, then no reaction occurs and the loop is incremented.
  (c) If j is an initiator, a random number r, $0 \leqslant r \leqslant 1$, is selected. If $r \leqslant P_I$, a reaction occurs; otherwise no reaction occurs.
  (d) If j is a radical (or a polymer chain with an active radical), a random neighbor is selected, where a neighbor is defined as an adjacent site in one of the six axial directions, and the label of the neighbor n determined. If the neighbor has an available bond (monomers can have one covalent bond, cross-linkers can have two), then a random number r, $0 \leqslant r \leqslant 1$, is selected. If $r \leqslant P_n$, P_n being the probability of a reaction occurring between the free radical and the particle type n, a reaction occurs; otherwise no reaction occurs.
  (e) If the reaction is to occur and n represents a site with no attachment to a free radical, then a bond is formed between j and n; this represents the propagation reaction. If n possesses a free radical, a bond is formed and the free radical is eliminated; this represents the termination by combination step.
  (f) If j represents an unbonded particle and j is not a void, an initiator, or an active racial, then a random neighbor n is selected. If n is a void, then the positions of n and j are switched. This allows diffusion of the constituents.
  (g) This procedure is repeated for N_{c_i} times.

The polymerization process is illustrated schematically in Fig. 3 and an example of a resulting configuration is given in Fig. 4.

At the conclusion of the kinetic Monte-Carlo process, the location of the site of each constituent and the connectivity of bonds forming the polymer chains is known. It is observed experimentally that upon completion of the polymerization process, a volume shrinkage of approximately 20% occurs upon removal of the quartz template. To account for this *densification* effect, bond potentials must be assigned to the polymerized etch barrier and a mathematical model must be formulated to describe the motion of the molecules due to the formation of the bonds. To this end, it is assumed that the bulk deformation of the polymer is a quasi-static process that can effectively be modeled using molecular statics.

2.2. Mechanics of the polymer – molecular statics

The goal of molecular statics is to minimize the global energy function as described in (2) with respect to admissible displacements. For the remainder of this work, it is assumed that the potentials are pair potentials and that there is no external loading, i.e. $\mathbf{f}_i = 0$. This leads to a system of nonlinear equations:

$$B(\mathbf{u};\mathbf{v}) = \sum_{j=1}^{N_0} \sum_{i=1}^{n_j} \frac{\partial E_{ij}}{\partial \mathbf{u}_j} \cdot \mathbf{v}_j = 0, \qquad (15)$$

where n_j is the number of particles neighboring particle j, and E_{ij} is the (pair) potential function between particles i and j. Letting $\mathbf{x}_j^0$ be the initial position of particle j, $\mathbf{x}_j = \mathbf{x}_j^0 + \mathbf{u}_j$ be the current position of molecule j, and $r_{ij} = \|\mathbf{x}_j - \mathbf{x}_i\|$ the Euclidean distance between particles i and j, then for all pair potentials

$$\frac{\partial E_{ij}}{\partial \mathbf{u}_j} = \frac{\partial E_{ij}(r_{ij})}{\partial r_{ij}} \frac{(\mathbf{x}_j^0 + \mathbf{u}_j) - (\mathbf{x}_i^0 + \mathbf{u}_i)}{\|(\mathbf{x}_j^0 + \mathbf{u}_j) - (\mathbf{x}_i^0 + \mathbf{u}_i)\|}. \qquad (16)$$

The term $\partial E_{ij}/\partial r_{ij}$ represents the magnitude of the force between particles i and j while the remaining term represents the direction of the force. Note that, even though the derivatives of the potential function may be linear, the second term induces a geometric nonlinearity.

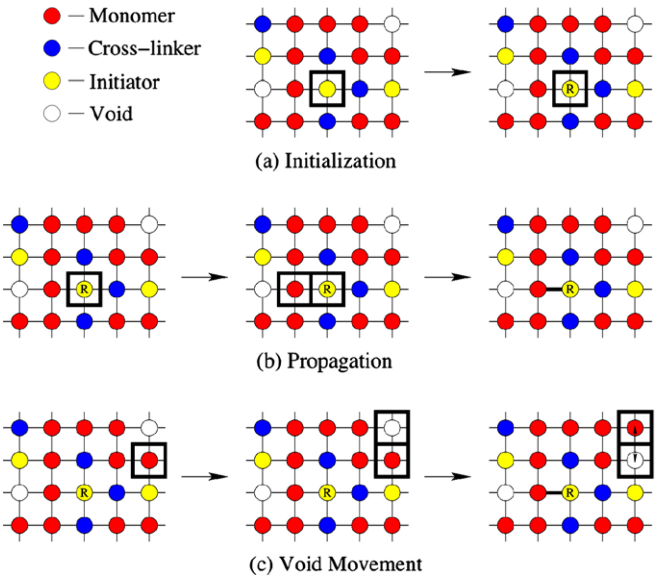

(a) Initialization

(b) Propagation

(c) Void Movement

Fig. 3. A schematic of the kinetic Monte-Carlo polymerization algorithm. *Initiation* – if an initiator is randomly selected that is not a free radical, then it is made a free radical if the reaction is determined to occur. This is depicted in (a) from left to right. *Propagation* – if a free radical is randomly selected, then a random neighbor is selected. If a bond has not been formed, then a bond is formed if the reaction is determined to occur. This is depicted in (b) from left to right. *Void diffusion* – if an unreacted particle is randomly selected, then a random neighbor is selected. If that neighbor is a void, then the cell location of the void and the neighbor is switched. This is depicted in (c) from left to right.

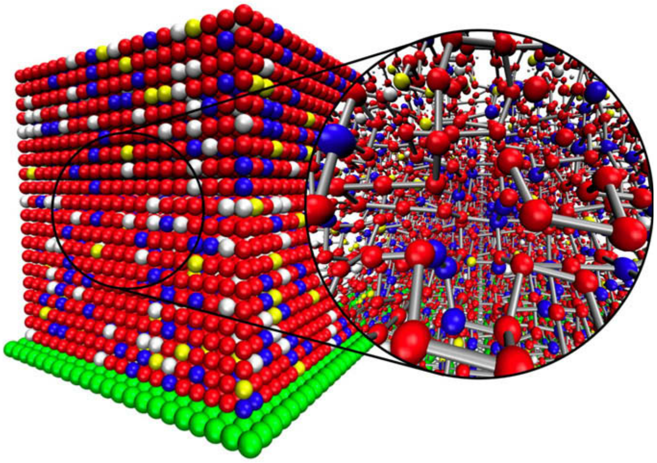

Fig. 4. A configuration generated by the kinetic Monte-Carlo polymerization algorithm with dimensions of 21 × 101 × 21. Green spheres denote the transfer layer particles, red the monomer 1 and monomer 2, blue the cross-linkers, yellow the initiators, and white denote voids. The zoomed portion shows the configuration of the covalent bonds following relaxation of the lattice. (For interpretation of the references to colour in this figure legend, the reader is referred to the web version of this article.)

The covalent bonds between molecules are modeled here with harmonic spring potentials:

$$E_{ij}^H = \frac{k_{ij}}{2}(r_{ij} - r_{ij}^0)^2, \qquad (17)$$

where k_{ij} is the spring stiffness and r_{ij}^0 is the unstretched length of the spring connecting molecules i and j. Weaker harmonic springs have also been used to describe van der Waal's interactions. The van der Waal's potentials are only assigned to the nearest neighbors and only 18 of the 26 neighbors are included. See Fig. 5. Tables 1 and 2 summarize the values of the spring constants used for the molecules discussed previously. The following notation is used: $(\cdot)^c$ represent parameters for covalent bonds and $(\cdot)^v$ are parameters for van der Waal's interactions. In this case, all of the covalent bonds are assigned the values $k_{ij}^c = 10.0$ and $r_{ij}^{0c} = 3.08$.

2.3. Numerical results

In this section, several results are shown illustrating both the character of solutions of the base model and the convergence properties of the algorithm used. Only representative results are shown here; see [6] for more examples and a more thorough discussion on the robustness of various algorithms. The algorithms for solving the problems are implemented in the software packages PETSc [4,3,5] and TAO [12]. In all cases discussed below, the relative residual decrease required for convergence of the nonlinear solver is a tolerance of 10^{-8}. All other parameters are the default parameters in the PETSc and TAO packages.

At this point, it is worth commenting that boundary conditions for large-scale molecular models are a perpetual problem, particularly for applications of the type described here where no periodicity or symmetry conditions are readily applicable. In the test problems described here, the lower boundary of the etch barrier can be best represented as a number of layers of a substrate polymer. In the examples discussed here, only one such layer is employed for simplicity.

A 10 × 10 × 10 polymer lattice is equilibrated using the inexact Newton trust-region approach. Fig. 6 shows convergence results and Fig. 7 shows the configurations for several Newton steps. Based on these images, it would seem that the first few Newton iterations capture the bulk deformation of the material and the ensuing steps adjust the small deformations of individual particles. Furthermore, based on the convergence behavior, a possible challenge with this problem may be that the minima are very closely spaced requiring many Newton iterations to find a minimum.

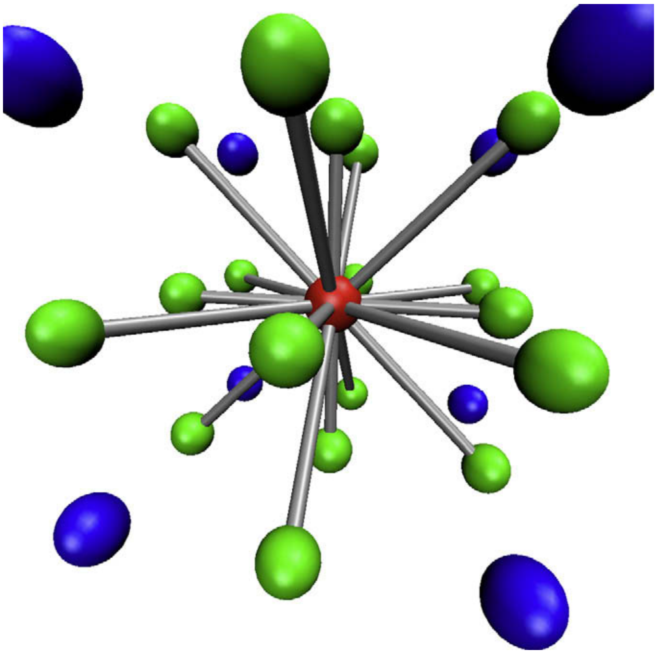

Fig. 5. The bonding configuration for each particle. The green particles represent neighboring particles which are allowed to bond to the red; they can be covalent or van der Waal's bonds. Blue particles are not allowed to bond to the red particle. (For interpretation of the references to colour in this figure legend, the reader is referred to the web version of this article.)

Table 1
Spring constants k_{ij}^v used for bonds between polymer molecules.

	M_1	M_2	XL	I	Substrate
M_1	1.1	0.8	1.2	0.9	1.0
M_2	0.8	1.0	0.7	1.3	1.0
XL	1.2	1.3	1.5	0.6	1.0
I	0.9	0.7	0.5	0.6	1.0
Substrate	1.0	1.0	1.0	1.0	

Table 2
Spring constants r_{ij}^{0v} used for bonds between polymer molecules.

	M_1	M_2	XL	I	Substrate
M_1	5.4	5.5	5.7	4.8	5.34
M_2	5.5	5.2	4.9	5.9	5.34
XL	5.7	5.9	5.3	5.8	5.34
I	4.8	4.9	5.8	5.1	5.34
Substrate	5.34	5.34	5.34	5.34	

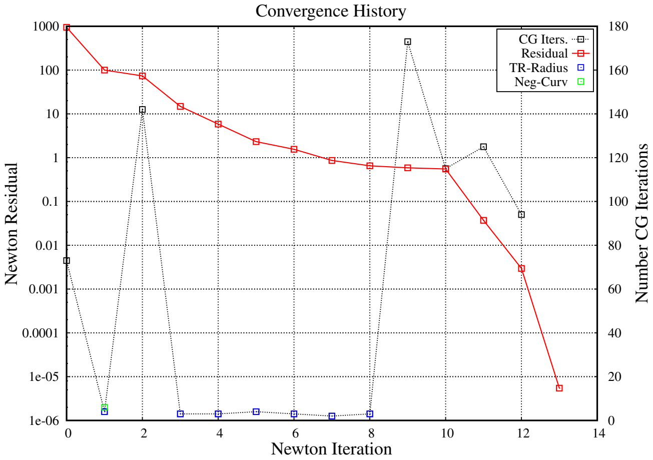

Fig. 6. Convergence behavior of a 10 × 10 × 10 polymer lattice using an inexact Newton with trust-region algorithm. The red curve shows the value of the residual (gradient) and the black curve is the number of C–G iterations required at each step. Note that the blue boxes show where the trust-region size restricted the size of the Newton step while black boxes mean the linear solver converged fully. The algorithm terminated successfully: the relative tolerance of the residual was reduced by the specified amount. (For interpretation of the references to colour in this figure legend, the reader is referred to the web version of this article.)

Consider now a 30 × 30 × 30 polymer lattice. Convergence curves are shown in Fig. 8. The convergence behavior is similar to the 10 × 10 × 10 case, but there are many more Newton iterations indicating that perhaps the energy function becomes less smooth as the dimension of the problem is increased, i.e. larger samples give many more possible local minima. This notion is also supported by the 110 × 110 × 110 lattice results shown in Figs. 9 and 10. This problem consists of over 4.1 million unknowns and was solved on 64 processors taking a total 65 CPU hours to solve. Indeed, over 3600 Newton iterations were required to attain equilibrium.

3. Development of a continuum model

A critical step in the multiscale modeling procedure developed here is the construction of a continuum model that represents events at larger scales than the base model, but is compatible to the base model in some sense. Generally, coarser-scale models may result from averaging the features of fine-scale models through various homogenization methods or ensemble-averaging techniques. In this case, a continuum model is chosen, but one

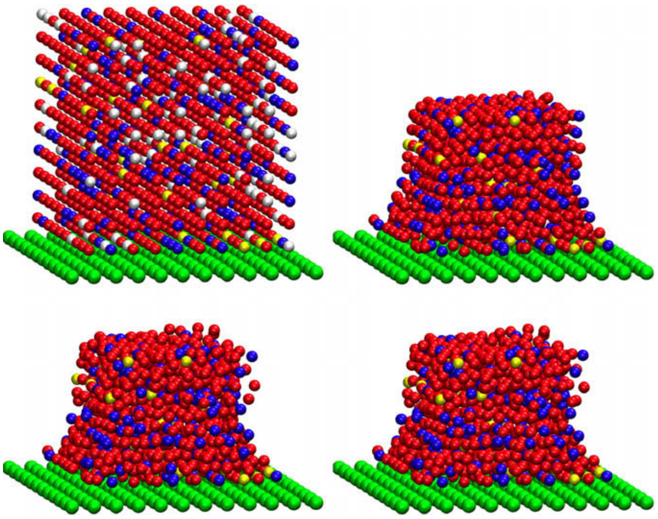

Fig. 7. Deformations of 10 × 10 × 10 polymer lattice using the inexact Newton with trust-region algorithm. Newton steps 0, 1, 5, and 13 are shown. All images of the base model deformations are rendered using visual molecular dynamics (VMD) [21].

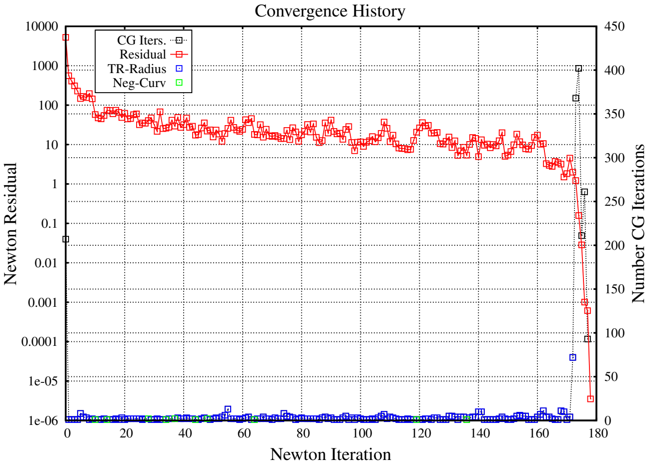

Fig. 8. The same information is contained in this figure as in Fig. 6 for the case of a 30 × 30 × 30 polymer lattice.

whose corresponding constitutive equation coefficients are unknown. A scheme is described below that is designed to determine these unknown coefficients using "virtual" (numerical) experiments that are performed on a representative volume element (RVE) of polymer material.

3.1. Virtual experiments on RVE's

The polymerization process described earlier does not involve any features that would lead to macroscale inhomogeneities or anisotropies, and the monomer and crosslinker constituents were designed to avoid or minimize rate effects. Thus, the assumption that the process leads to a material behaving as an amorphous elastomer seems reasonable. The macroscale model of the polymerized etch barrier is then that of a homogeneous, isotropic, hyperelastic material with a stored energy per unit volume W relative to a reference configuration $\Omega_0 \subset \mathbb{R}^3$.

Let $\mathbf{X}$ denote the labels of material particles of the body, with X_i the Cartesian coordinates of particle positions in the reference configuration. The motion $\boldsymbol{\varphi} : \overline{\Omega}_0 \to \overline{\Omega}$ is a differentiable, orientation preserving map that takes particles into positions $\mathbf{x} = \boldsymbol{\varphi}(\mathbf{X})$ in the current ("deformed") configuration, and $\mathbf{F}(\mathbf{X}) = \nabla_{\mathbf{X}}\boldsymbol{\varphi}$ is the deformation gradient tensor. The right Cauchy–Green deformation tensor is denoted $\mathbf{C} = \mathbf{F}^T\mathbf{F}$. A fundamental condition on the stored energy function W is that it be form-invariant under all changes in the observer frame of reference, which, generally, means that W must depend on invariants of the deformation. One way of guaranteeing this invariance is to write W as a function of the principal invariants of $\mathbf{C}$:

$$W = W(I_1, I_2, I_3), \tag{18}$$

where

$$\begin{aligned} I_1 &= \mathrm{tr}\mathbf{C} = \lambda_1 + \lambda_2 + \lambda_3, \\ I_2 &= \frac{1}{2}(\mathrm{tr}\mathbf{C})^2 - \frac{1}{2}tr(\mathbf{C})^2 \\ &= \lambda_1\lambda_2 + \lambda_1\lambda_3 + \lambda_2\lambda_3, \\ I_3 &= \det\mathbf{C} = \lambda_1\lambda_2\lambda_3, \end{aligned} \tag{19}$$

and λ_i are the principal stretches of material line elements.

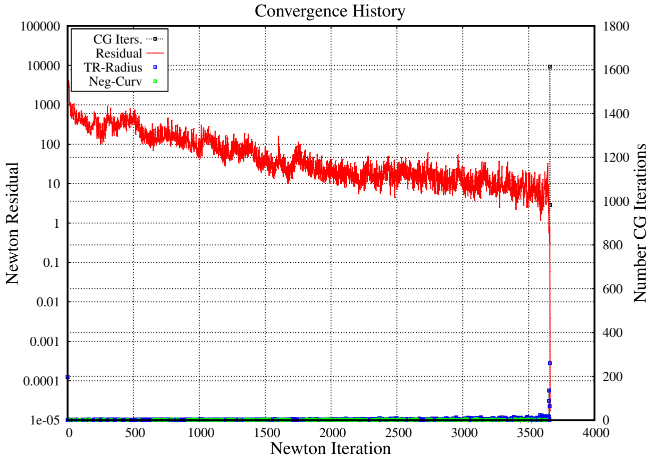

Fig. 9. The same information is contained in this figure as in Fig. 6 for the case of a 110 × 110 × 110 polymer lattice.

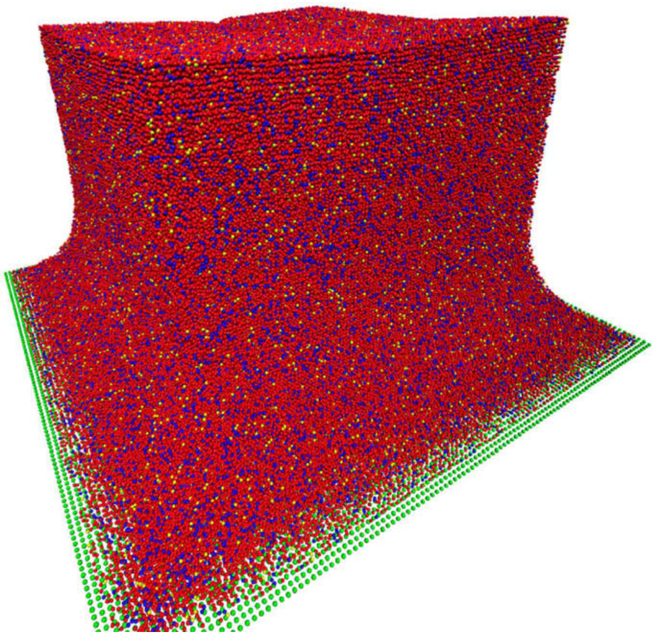

Fig. 10. An equilibrium configuration of a 110 × 110 × 110 polymer lattice.

The following forms for W are considered:

$$W = C_1(I_1 - 3 - \ln\sqrt{I_3}) + C_2(\sqrt{I_3} - 1)^2,$$
$$W = C_1(I_1 - 3) + C_2(I_2 - 3) + C_3(\sqrt{I_3} - 1)^2 - (2C_1 + 4C_2)\ln\sqrt{I_3}. \quad (20)$$

These equations represent the compressible versions of the classical Neo–Hookean and Mooney–Rivlin materials [16]. The development of these constitutive equations is inspired by early work in the statistical mechanics of polymer networks and to arguments related to macroscale experiments on elastomers [31,32].

The virtual testing procedure, depicted in Fig. 11 involves the following steps:

(i) A cube $D \subset \mathbb{R}^3$ of polymerized material, initially of size $L_0 \times L_0 \times L_0$ with $N_x \times N_y \times N_z = N_D$ particles, is generated using the kinetic Monte-Carlo algorithm described in Section 2.1, and is allowed to assume a relaxed (densified) equilibrium configuration after constraints sufficient to eliminate rigid translations and rotations are applied. The cube D is the initial RVE.

(ii) Uniform tractions are applied over opposite faces of the cube by assigning values of the net force on molecules residing on the near-planar boundaries of D.

(iii) The resulting principal stretches $\lambda_1, \lambda_2, \lambda_3$ are calculated by computing the length of the stretched RVE and by taking the ratio with the initial length of the relaxed RVE: $\lambda_1 = L^x/L^x_0$, etc. These lengths are calculated by averaging the positions of the particles on each face and computing the difference of these averages. Furthermore, the Jacobian $J = \det\mathbf{F} = \sqrt{\lambda_1\lambda_2\lambda_3}$ is measured (calculated) from the RVE.

(iv) The total energy E_D in D is computed in the relaxed and stretched configurations.

(v) The total energy density in D is equated to the continuum stored energy density in D:

$$\frac{E_D}{V_0} = W. \quad (21)$$

Furthermore, for the cases of uniaxial and biaxial extension, exact solutions can be formulated for the continuum model and the measured stretches λ_i can be compared to the expected values.

Some important aspects of this process are noted:

(i) The constants determined by this process should be independent of the size of the RVE; thus the dimension of the domain D, i.e. $N_x \times N_y \times N_z$, should be increased until the computed values of the material parameters do not change.

(ii) A single molecular model of the RVE represents only one realization of the polymeric structure. Thus, a large number of such realizations should be generated to determine the statistical variations of the material parameters with sufficient accuracy.

(iii) The form of W assumed in the process should represent a stable characterization of the material, relatively insensitive to small perturbations in the molecular model.

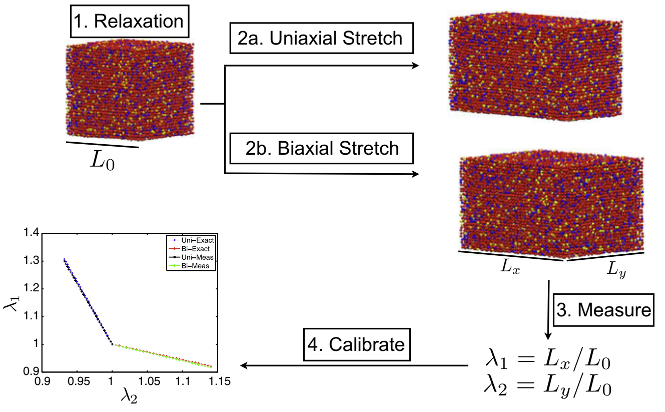

Fig. 11. RVE testing procedure. Step 1. Relaxation of the polymer lattice. Step 2. Deformation (uniaxial and biaxial stretches). Step 3. Measurements of $V, \lambda_1, \lambda_2, \lambda_3, E$. Step 4. Determination of the continuum parameters by curve fitting.

3.2. Numerical RVE experiments

3.2.1. Determination of RVE size

Following the previous discussion, the size of the RVE must be determined so that the constants computed for the continuum model are stable with respect to increase in the RVE size. To determine the RVE size, an RVE is subjected either to uniaxial extension with lateral contraction or biaxial extension. Since the material behaves as an isotropic homogeneous material on the scale of the RVE, it is expected that certain symmetries will hold. In the case of uniaxial extension in the x-direction, $\lambda_2 = \lambda_3$. In biaxial extension in the x-direction and y-direction, $\lambda_1 = \lambda_2$. Furthermore, in both cases, the ratio of the volume change $V/V_0 = \sqrt{I_3}$, and it is expected that the energy density should converge as the RVE size is increased. Thus, in the RVE experiment, $\lambda_1, \lambda_2, \lambda_3$ are computed by taking the ratio of the deformed length in each direction with the original length, and the volume of both the deformed and original configurations are calculated. This procedure was executed on polymer RVE's of size $10 \times 10 \times 10$, $20 \times 20 \times 20$, and $30 \times 30 \times 30$. Fig. 12 shows the energy density and the volume comparison for uniaxial loading tests while Fig. 13 shows the symmetry tests for uniaxial and biaxial loadings.

As can be seen, as the RVE size is increased to $30 \times 30 \times 30$, the properties converge as expected to quite tight tolerances. The only exception is the case of symmetry of the biaxial loading of the RVE. Here, the curves do not converge as expected, but the ratio is still very close to one and, thus, is considered acceptable. Based on these numerical experiments, an RVE size of $30 \times 30 \times 30$ is considered adequate to determine the continuum coefficients for each realization of the polymer structure.

3.2.2. Parameter fit from RVE Data

With the RVE size determined and data collected from deformations on the RVE, a least-squares fitting procedure is used to determine the parameters for the continuum constitutive equation. There are three sets of data used to fit the parameters: the energy density for both uniaxial and biaxial deformations, the relationship between λ_2 and λ_3 in the unaxial deformation, and the relationship between λ_1 and λ_2 in the biaxial deformation for the different loading values. In the first case, this merely means fitting $W(I_1, I_2, I_3) = E/V_0$ where I_1, I_2, I_3 are computed from the measured stretches. In the latter two cases, these relationships come from the exact solution to the uniaxial and biaxial deformations. For this fitting procedure, the body is stretched 30% in 20 incremental steps for the uniaxial and biaxial deformations. The resulting parameters are collected in Table 3 and the corresponding curve fits are shown in Figs. 14 and 15.

3.3. Finite element formulation

Here, we introduce the classical formulation for finite elements in nonlinear elasticity in order to lay down notation for subsequent use in the formulation of the coupled model.

Let $\Omega_0 \subset \mathbb{R}^3$ be an open, connected, bounded set representing the reference configuration of an undeformed body $\mathscr{B}$ in free space

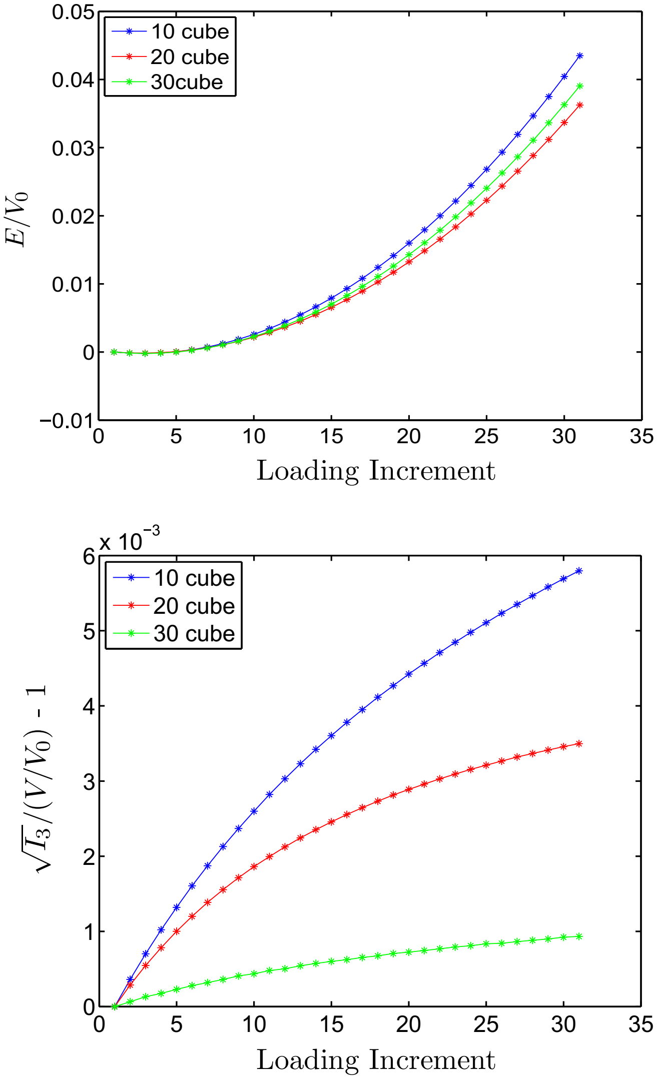

Fig. 12. RVE's of the polymer are deformed under uniaxial loading. The top curve illustrates the energy density for the 10, 20, and 30 cubes while the bottom curve shows the ratio $\sqrt{I_3}/(V/V_0)$; if the polymer was perfectly symmetric, this ratio would be one.

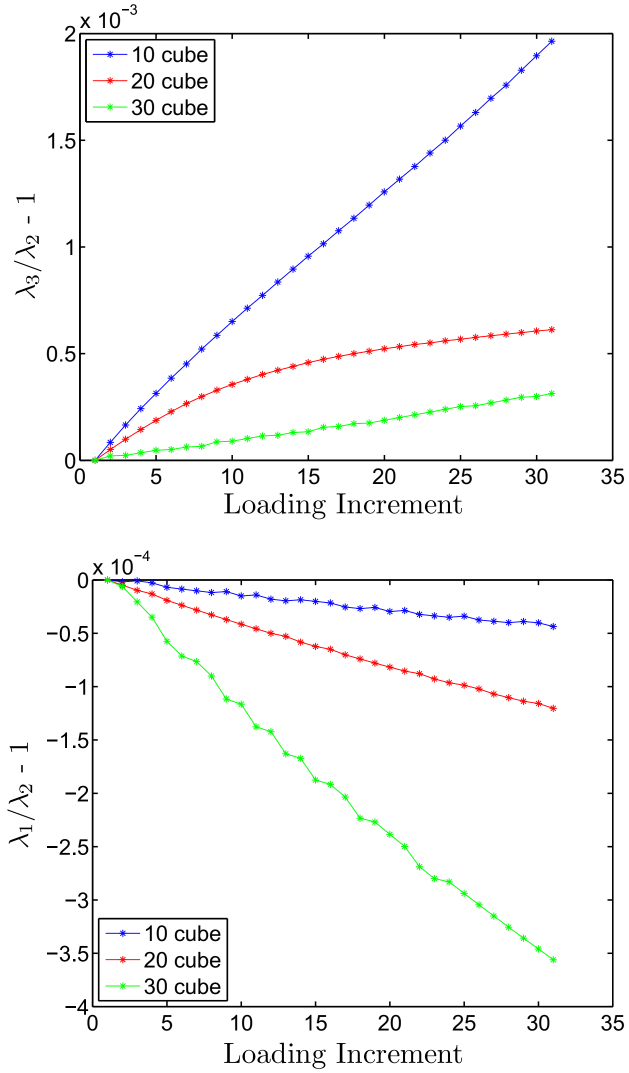

Fig. 13. RVE's of the polymer are deformed under loading. The top curve illustrates the ratio λ_2/λ_3 for the 10, 20, and 30 cubes under uniaxial loading; if the polymer was perfectly symmetric, the ratio would be one. The bottom set of curves correspond to the cubes under biaxial loading and shows the ratio λ_1/λ_2. Again, if the RVE was perfectly symmetric, this value would be one.

with boundary Γ. Let the material points of $\mathscr{B}$ be labeled by $\boldsymbol{X} \in \mathbb{R}^3$. Under the action of body forces $\boldsymbol{b}$ acting on all of Ω_0, applied tractions $\boldsymbol{t}$ acting on Γ_N, the body undergoes a motion $\boldsymbol{\varphi}(\boldsymbol{X}) : \Omega_0 \rightarrow \Omega$, where Ω is the current configuration.

Let $\Pi(\boldsymbol{\varphi})$ be the total energy function of body $\mathscr{B}$. Furthermore, let $W(\nabla\boldsymbol{\varphi})$ be the given stored energy density function of the body. Then

$$\Pi_c(\boldsymbol{\varphi}) = \int_{\Omega_0} W(\nabla\boldsymbol{\varphi}) d\mathbf{X} - \int_{\Omega_0} \rho_0 \mathbf{b}\cdot\boldsymbol{\varphi} d\mathbf{X} - \int_{\Gamma_N} \mathbf{t}\cdot\boldsymbol{\varphi} d\Gamma_N, \tag{22}$$

where $d\mathbf{X} = dX_1 dX_2 dX_3$.

The goal is to solve the following minimization problem:

$$\text{Find} \quad \boldsymbol{\varphi}^* \in V : \Pi_c(\boldsymbol{\varphi}^*) = \min_{\boldsymbol{\varphi}\in V} \Pi_c(\boldsymbol{\varphi}), \tag{23}$$

where

$$V = \{\boldsymbol{\varphi} : \overline{\Omega}_0 \rightarrow \mathbb{R}^3 : W(\nabla\boldsymbol{\varphi}) \in L^1(\Omega_0), \quad \det\ \nabla\boldsymbol{\varphi} > 0 \text{ a.e. in } \Omega_0\}. \tag{24}$$

See [16].

The function $\boldsymbol{\varphi}$ is approximated by tri-linear hexahedra. Throughout, repeated indices are to be summed according to the Einstein summation convention. If repeated indices are not to be summed, the indices will be underlined: $\underline{i}$. Lowercase $i, j, k, \ldots$ denote spatial coordinate indices, while uppercase $I, J, K, \ldots$ denote material coordinate indices. The indices A, B denote global basis function indices. Then, the discretized gradient and Hessian of the energy function are

$$\begin{aligned} \frac{\partial \Pi_c}{\partial d_{iA}} &= \int_{\Omega_0} F_{\underline{i}I} S_{IJ} N^{\underline{i}}_{A,J} d\mathbf{X} - \int_{\Omega_0} \rho_0 B_{\underline{i}} N^{\underline{i}}_{A} d\mathbf{X} - \int_{\Gamma_N} T_{\underline{i}} N^{\underline{i}}_{A} d\Gamma_N \\ \frac{\partial^2 \Pi_c}{\partial d_{iA} \partial d_{jB}} &= \int_{\Omega_0} N^{\underline{j}}_{B,I} S_{IJ} N^{\underline{j}}_{A,J} + F_{\underline{i}I} C_{IJKL} F_{\underline{j}K} N^{\underline{i}}_{A,J} N^{\underline{j}}_{B,L} d\mathbf{X} \end{aligned} \tag{25}$$

Table 3
Results of parameter fit for the compressible Neo–Hookean and the compressible Mooney–Rivlin materials based upon the RVE experiments on one representative sample of a 30 × 30 × 30 polymer lattice.

Model	C_1	C_2	C_3
Compressible Neo–Hookean	0.72	0.57	
Compressible Mooney–Rivlin	0.67	0.23	0.22

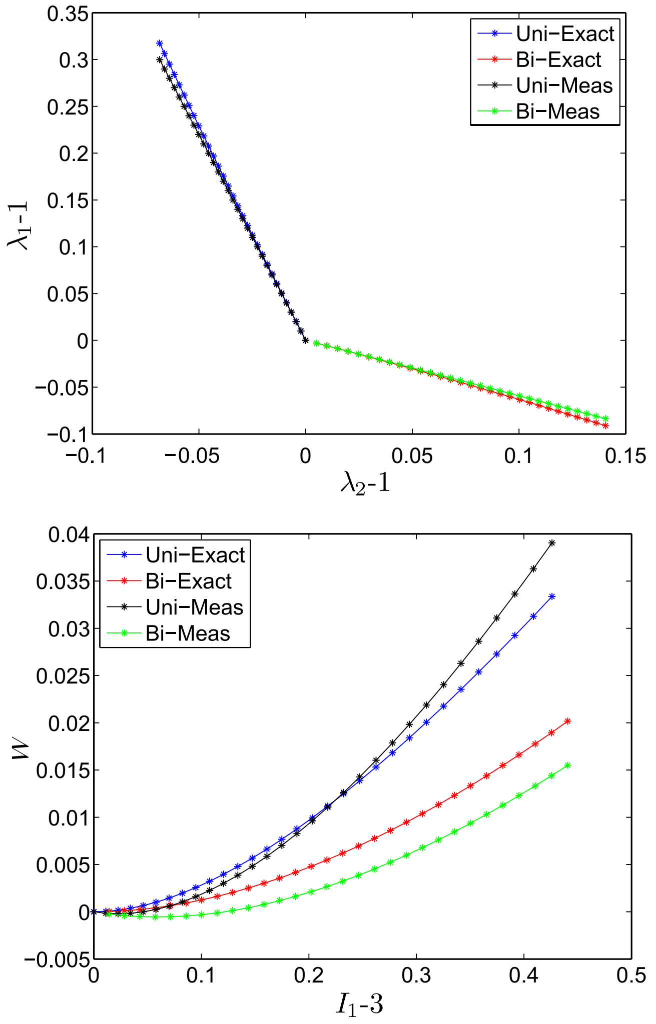

Fig. 14. Resulting parameter fits for the compressible Neo–Hookean material based upon measurements from a 30 × 30 × 30 polymer RVE. The top figure shows the values expected for λ_1, based on λ_2, from the exact solution to the uniaxial and biaxial extension problems compared to those measured in the numerical experiment. Similarly, the bottom figure compares the value expected from the compressible Neo–Hookean energy density equation and the measured energy density on the RVE.

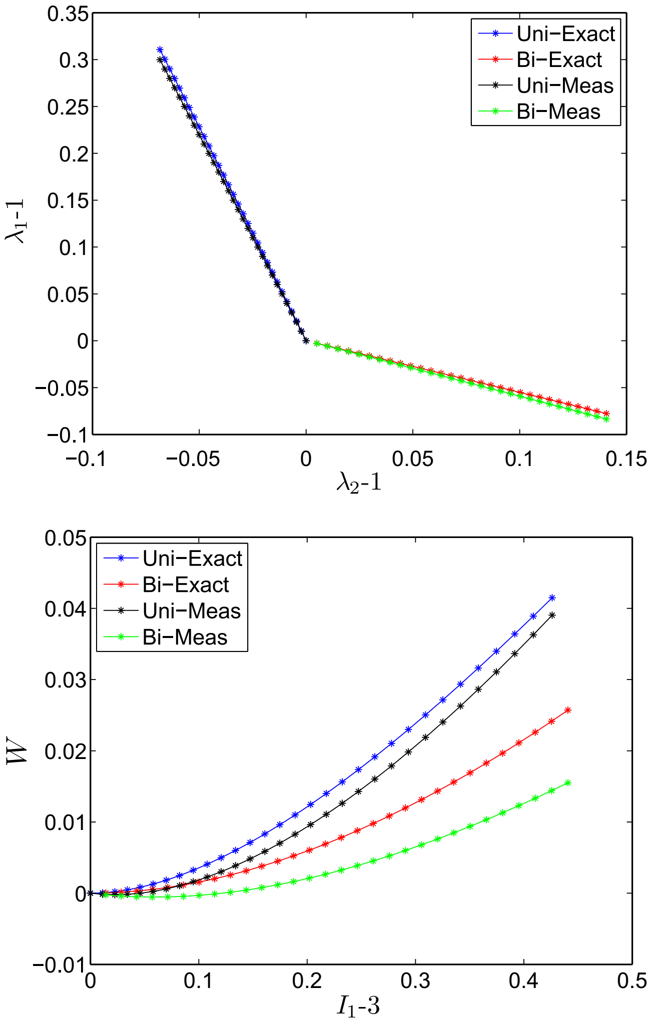

Fig. 15. Same as Fig. 14 for the compressible Mooney–Rivlin material.

where d_{iA} are the coefficients of the shape functions approximating $\boldsymbol{\varphi}_i$, S_{IJ} is the second Piola–Kirchoff stress tensor, and C_{IJKL} is the elasticity tensor. Both quantities can be written in terms of the invariants of the deformation and are given by

$$S_{IJ} = 2\left(\frac{\partial W}{\partial I_1}\delta_{IJ} + \frac{\partial W}{\partial I_2}(I_1\delta_{IJ} - C_{IJ}) + \frac{\partial W}{\partial I_3}\left(I_3 C_{IJ}^{-1}\right)\right), \tag{26}$$

and

$$\begin{aligned} C_{IJKL} = 4\Bigg(&\frac{\partial^2 W}{\partial I_1^2}(\delta_{IJ}\delta_{KL}) + \frac{\partial^2 W}{\partial I_2^2}(I_1\delta_{IJ}(I_1\delta_{KL} - C_{KL}) + C_{IJ}(\delta_{KL} - C_{KL})) \\ &+ \frac{\partial^2 W}{\partial I_3^2}(I_3^2 C_{IJ}^{-1} C_{Kl}^{-1}) + \frac{\partial^2 W}{\partial I_1 \partial I_2}(I_1\delta_{IJ}(\delta_{KL} - C_{KL}) + I_1\delta_{KL}(\delta_{IJ} - C_{IJ})) \\ &+ \frac{\partial^2 W}{\partial I_1 \partial I_3} I_3(\delta_{IJ} C_{KL}^{-1} + C_{IJ}^{-1}\delta_{KL}) + \frac{\partial^2 W}{\partial I_2 \partial I_3} I_3(C_{KL}^{-1}(I_1\delta_{IJ} - C_{IJ}) \\ &+ C_{IJ}^{-1}(I_1\delta_{KL} - C_{KL})) + \frac{\partial W}{\partial I_2}(\delta_{IJ}\delta_{KL} - \delta_{IK}\delta JL) \\ &+ \frac{\partial W}{\partial I_3} I_3\left(C_{IJ}^{-1}C_{KL}^{-1} - \frac{1}{2}(C_{IK}^{-1}C_{JL}^{-1} + C_{IL}^{-1}C_{JK}^{-1})\right)\Bigg), \end{aligned} \tag{27}$$

where δ_{IJ} is the Kronecker delta. The gradient and Hessian of the energy function are provided to the software packages TAO [12] and PETSc [4,3,5] which use inexact Newton with trust-region to find a minimum of the energy Π_c.

3.4. Initial strain formulation

The difficulty here is that the equations of continuum mechanics do not inherently contain the stretch in the lattice: by default the reference configuration of the continuum body is strain free. Thus, additional information must be supplied to provide this initial strain to the continuum body. Consider the case of the lattice model which is composed of a network of harmonic springs. Implicit in the spring model is a reference length to which any deformation is compared. Thus, when the bonds are formed during the polymerization process and the molecules form a perfect lattice, the springs are stretched from the reference length and, therefore, the dimensions of the body shrink under the action of the stretched springs and not due to external loading. See for example, Fig. 7.

The main idea to incorporate this information into the continuum model is to consider three configurations of a material body: the reference configuration Ω_0 in which the polymer assumes the prismatic form defined by the lattice boundaries after the polymerization process (generally cubic), the current configuration Ω in which boundary conditions are imposed and densification takes place (due to the initial strain), and a "strain-free" configuration

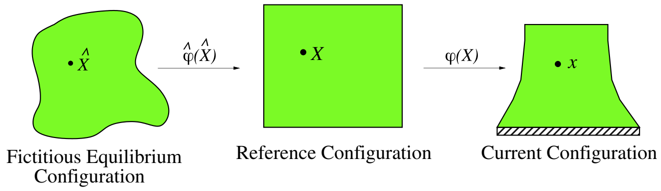

Fig. 16. Incorporating initial strain into nonlinear elasticity.

$\hat{\Omega}$ in which no external forces act on the body so it is in equilibrium with zero boundary tractions. The latter shall be referred to as the *fictitious equilibrium configuration*.

Let $\mathbf{X}$ denote a material point in the reference configuration and $\hat{\mathbf{X}}$ the material point in the fictitious equilibrium configuration. These are related by a differentiable, invertible map $\hat{\varphi} : \overline{\hat{\Omega}} \to \overline{\Omega_0}$ such that $\mathbf{X} = \hat{\boldsymbol{\varphi}}(\hat{\mathbf{X}})$. The spatial positions of $\mathbf{x}$ in the current configuration are $\mathbf{x} = \boldsymbol{\varphi}(\mathbf{X}), \boldsymbol{\varphi} : \overline{\Omega_0} \to \overline{\Omega}$. Fig. 16 represents this process schematically. Thus

$$\mathbf{x} = \varphi \circ \hat{\varphi} = \boldsymbol{\varphi}(\hat{\boldsymbol{\varphi}}(\hat{\mathbf{X}})), \tag{28}$$

and, using the chain rule:

$$\nabla_{\hat{\mathbf{X}}}\mathbf{x} = \nabla_{\mathbf{X}}\varphi(\mathbf{X})\nabla_{\hat{\mathbf{X}}}\hat{\varphi}(\hat{\mathbf{X}}) = \mathbf{F}\hat{\mathbf{F}}. \tag{29}$$

Therefore, the gradient $(25)_1$ and Hessian $(25)_2$ become

$$\begin{aligned}\frac{\partial \Pi}{\partial d_{iA}} &= \int_{\Omega_0} F_{\underline{i}K}\hat{F}_{KI}S_{IJ}N^{\underline{i}}_{A,M}\hat{F}_{MJ}d\mathbf{X} - \int_{\Omega_0} \rho_0 B_{\underline{i}}N^{\underline{i}}_{A}d\mathbf{X} - \int_{\Gamma_N} T_{\underline{i}}N^{\underline{i}}_{A}d\Gamma_N,\\ \frac{\partial^2 \Pi}{\partial d_{iA}\partial d_{jB}} &= \int_{\Omega_0} N^{\underline{j}}_{B,K}\hat{F}_{KI}S_{IJ}N^{\underline{i}}_{A,M}\hat{F}_{MJ}d\mathbf{X}\\ &\quad + \int_{\Omega_0} F_{\underline{i}M}\hat{F}_{MI}C_{IJKL}F_{\underline{j}N}\hat{F}_{NK}N^{\underline{i}}_{A,O}\hat{F}_{OJ}N^{\underline{j}}_{B,P}\hat{F}_{PL}d\mathbf{X}\end{aligned} \tag{30}$$

The task now is to supply $\hat{\mathbf{F}}$. In general, $\hat{\mathbf{F}} = \hat{\mathbf{F}}(\hat{\mathbf{X}})$, but in the present case, $\hat{\mathbf{F}}$ is the result of a homogeneous deformation of the RVE of the form:

$$\hat{\mathbf{F}} = \lambda\mathbf{I}, \tag{31}$$

where $\mathbf{I}$ is the identity matrix and λ is a constant to be determined. The form (31) is justified for the case of the polymer under consideration as the bonds are random in direction so that there is no preferred direction for the deformation. Therefore, numerical experiments on RVE's of the polymer material can be used to determine the constant λ. Note that, in the case of $\hat{\mathbf{F}} = \lambda\mathbf{I}$

$$\hat{\mathbf{C}} = \hat{\mathbf{F}}^T\hat{\mathbf{F}} = \lambda^2\mathbf{I}, \tag{32}$$

so that $\lambda^2 = \lambda_1 = \lambda_2 = \lambda_3$. Thus, the stretch of the body can be measured on an RVE of polymer when being equilibrated; that is, the stretch from the equilibrated configuration to the lattice configuration. Actually, what is measured is the inverse λ^{-1} since in the molecular RVE experiments, the lattice shrinks from the cubic reference configuration to the relaxed "fictitious equilibrium configuration". Fig. 17 shows an example of the incorporation of initial strain into the finite element formulation.

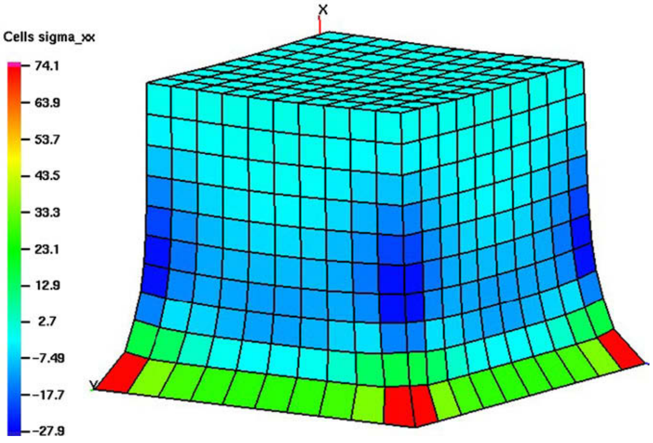

Fig. 17. A 1000 element simulation of a compressible Mooney–Rivlin material subjected to initial strain. In this case, $\lambda = 1.25$.

4. Arlequin coupling

This section details the development of a general scheme to systematically couple particle and continuum models in order to produce surrogates of the molecular base model. The strategy involves enforcing the displacement and derivative constraints between the two models. The constraints are achieved using Lagrange multipliers on a region of overlap between the continuum and particle models. This scheme is an adaptation of the Arlequin method [8,10,11,9] used for coupling two continuum models with differing scales of finite element discretization (a global coarse mesh and a local fine mesh). A mathematical development is given in [7] showing well-posedness for a one-dimensional problem coupling a harmonic spring model with a linearly elastic rod. Here, we extend the formulation to the coupling of the three-dimensional, nonlinear polymer model and the nonlinear, elastic continuum model discussed previously. Some details of the solution algorithm are presented followed by several numerical experiments illustrating the behavior of the solutions.

4.1. Continuous formulation

Let $\Omega \subset \mathbb{R}^3$ be open and bounded. Let $\Omega_c \subset \Omega$ be the continuum region of the body and let $\Omega_d \subset \Omega$ be the region containing M discrete particles (representing the lattice polymer model in this context). Let $\Omega_o = \Omega_c \bigcap \Omega_d$ be the region of overlap (see Fig. 18) and let

$$\begin{aligned}V_c &= \left\{\mathbf{v} : \Omega_c \to \mathbb{R}^3 : \left|\int_{\Omega_c} W(\nabla\mathbf{u})d\mathbf{x}\right| < \infty, \gamma_0\mathbf{v} = 0 \text{ on } \Gamma^D_c\right\},\\ V_d &= \{\mathbf{z} \in \mathbb{R}^{3M} : \mathbf{z} = 0 \text{ on } \Gamma^D_d\},\\ V_o &= \{\boldsymbol{\mu} \in H^1(\Omega_o)^3\}.\end{aligned} \tag{33}$$

Then, the Arlequin method proposes to solve the following saddle point problem:

$$\boxed{\inf_{(\mathbf{v},\mathbf{z})\in V_c\times V_d} \sup_{\boldsymbol{\mu}\in V_o} L(\mathbf{v},\mathbf{z},\boldsymbol{\mu}),} \tag{34}$$

where

$$L(\mathbf{v},\mathbf{z},\boldsymbol{\mu}) = E_c(\mathbf{v}) + E_d(\mathbf{z}) + b(\boldsymbol{\mu},(\mathbf{v},\mathbf{z})), \tag{35}$$

and

$$\begin{aligned}E_c(\mathbf{v}) &= \int_{\Omega_c} \alpha_c W(\nabla\mathbf{v})d\mathbf{X},\\ E_d(\mathbf{z}) &= \sum_{m=1}^{M}\sum_{n=1}^{n_m} \alpha_d E_{mn}(\|\mathbf{x}_m - \mathbf{x}_n\|) - \sum_{m=1}^{M} \mathbf{f}\cdot(\mathbf{x}_m - \mathbf{x}^0_m),\\ b(\boldsymbol{\mu},(\mathbf{v},\mathbf{z})) &= \int_{\Omega_o} \boldsymbol{\mu}\cdot(\mathbf{v} - I\mathbf{z}) + \nabla\boldsymbol{\mu} : \nabla(\mathbf{v} - I\mathbf{z})d\mathbf{X},\\ \alpha_c, \alpha_d &\in \mathbb{R} : \alpha_c + \alpha_d = 1 \text{ in } \Omega,\\ \alpha_c &= \begin{cases} 1 & \text{in } \Omega_c/\Omega_o,\\ 0 & \text{in } \Omega_d,\end{cases}\\ I &: V_d \to V_c,\end{aligned} \tag{36}$$

where $\mathbf{x}_m$ is the position of particle m and $I : V_d \to V_c$ is the piecewise tri-linear interpolation operator. Fig. 19 illustrates the weighting functions α_c and α_d for the one-dimensional case. In particular,

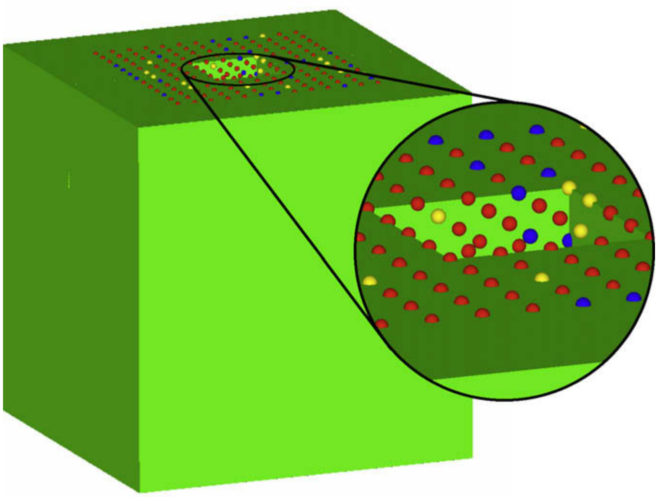

Fig. 18. Example of a geometry for the Arlequin method. The solid green represents the continuum model while the red, blue, and yellow particles represent monomer, cross-linker, and initiator, respectively. Notice that the zoomed shows the particle region, while the particles contained in the green region define the overlap region. (For interpretation of the references to colour in this figure legend, the reader is referred to the web version of this article.)

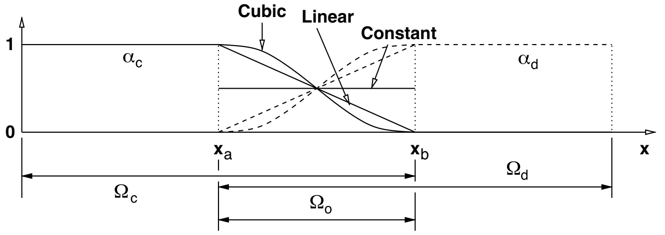

Fig. 19. Examples of α_c and α_d in one-dimension. Constant, linear, and cubic weighting functions are shown in the overlap region.

note the many choices in the overlap region (only the constant case is considered here).

4.2. Discrete formulation

Let $V_c^h \subset V_c$ and $V_o^h \subset V_o$ be finite-dimensional subspaces produced by discretizations of the continuum and Lagrange multiplier function spaces (see Fig. 20). In all examples that follow, the Lagrange multiplier finite elements will correspond to the continuum finite elements in the overlap region. The discrete formulation is as follows:

$$L(\mathbf{u}^h, \mathbf{x}, \boldsymbol{\lambda}^h) = \inf_{(\mathbf{v}^h, \mathbf{z}) \in V_c^h \times V_d} \ \sup_{\boldsymbol{\mu}^h \in V_o^h} L(\mathbf{v}^h, \mathbf{z}, \boldsymbol{\mu}^h), \tag{37}$$

where, as before

$$L(\mathbf{v}^h, \mathbf{z}, \boldsymbol{\mu}^h) = E_c(\mathbf{v}^h) + E_d(\mathbf{z}) + b(\boldsymbol{\mu}^h, (\mathbf{v}^h, \mathbf{z})). \tag{38}$$

Let N_A^i represent the finite element basis functions for the continuum model, A being the global node number and i the component of the vector (i.e. x, y, z), N_B^i the basis for the lagrange multipliers, and N_m^i the basis functions for interpolating the particles in Ω_o. Then,

$$u_i^h = \sum_{A=1}^{N_c} d_{\underline{i}A} N_A^{\underline{i}}, \quad \lambda_i^h = \sum_{B=1}^{N_l} l_{\underline{i}B} N_B^{\underline{i}}, \quad Ix_i = \sum_{m=1}^{N_l} x_{\underline{i}m} N_m^{\underline{i}}. \tag{39}$$

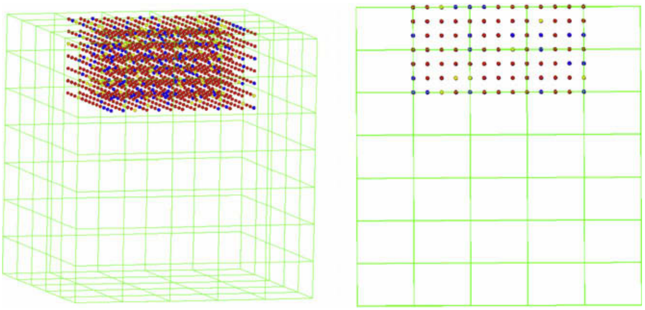

Fig. 20. The discretization of the geometry in Fig. 18 from an angle view and a side view.

Thus, the Lagrangian can be rewritten as

$$\begin{aligned} L(d_{iA}, x_{im}, l_{iB}) = & \int_{\Omega_c} \alpha_c W\left(\nabla\left(\sum_{A=1}^{N_c} d_{\underline{i}A} N_A^{\underline{i}}\right)\right) d\mathbf{X} \\ & - \int_{\Gamma_c^N} T_i \left(\sum_{A=1}^{N_c} d_{\underline{i}A} N_A^{\underline{i}}\right) d\Gamma_N \\ & + \sum_{m=1}^{M} \sum_{n=1}^{N_m} \alpha_d E_{mn}(\|x_{im} - x_{in}\|) - \sum_{m=1}^{M} f_{im}(x_{im} - x_{im}^0) \\ & + \int_{\Omega_o} \left(\sum_{B=1}^{N_l} l_{\underline{i}B} N_B^{\underline{i}}\right)\left(\sum_{A=1}^{N_c} d_{\underline{i}A} N_A^{\underline{i}} - \sum_{m=1}^{N_l} x_{\underline{i}m} N_m^{\underline{i}}\right) d\mathbf{X}. \end{aligned} \tag{40}$$

A necessary condition for a saddle point is that the derivative be zero. In particular, set

$$\frac{\partial L}{\partial d_{jD}} = 0, \quad \frac{\partial L}{\partial x_{im}} = 0, \quad \frac{\partial L}{\partial l_{jE}} = 0. \tag{41}$$

Thus, (41) yields the following system of nonlinear equations:

$$\begin{aligned} & \int_{\Omega_c} \alpha_c S_{IJ} F_{\underline{i}I} N_{D,J}^{\underline{i}} d\mathbf{X} + \int_{\Omega_o} \left(\sum_{B=1}^{N_l} l_{\underline{j}B} N_{B,I}^{\underline{j}}\right) N_{D,I}^{\underline{j}} d\mathbf{X} = \int_{\Gamma_c^N} T_{\underline{j}} N_D^{\underline{j}} d\Gamma_N \\ & \quad \sum_{n=1}^{N_m} \alpha_d E'_{nm}(\|x_{\underline{im}} - x_{\underline{in}}\|) \frac{(x_{\underline{im}} - x_{\underline{in}})}{\|x_{\underline{im}} - x_{\underline{in}}\|} \\ & \quad - \int_{\Omega_o} \left(\sum_{B=1}^{N_l} l_{\underline{j}B} N_{B,I}^{\underline{j}}\right) N_{m,I}^{\underline{i}} d\mathbf{X} = f_{im} \\ & \quad \int_{\Omega_o} N_{E,I}^{\underline{j}} \left(\sum_{A=1}^{N_c} d_{\underline{i}A} N_A^{\underline{i}} - \sum_{m=1}^{N_I} x_{\underline{i}m} N_m^{\underline{i}}\right) d\mathbf{X} = 0. \end{aligned} \tag{42}$$

Note that the initial strain can easily be incorporated into the continuum as in Section 3.4.

The Newton with line search algorithm is used to solve the above system. Repeating the differentiation procedure to arrive at (42), the Jacobian is

$$\mathbf{J} = \begin{bmatrix} J_c & 0 & J_{\lambda c} \\ 0 & J_d & J_{\lambda d} \\ J_{\lambda c}^T & J_{\lambda d}^T & 0 \end{bmatrix}, \tag{43}$$

where

$$\begin{aligned} J_c &= \frac{\partial^2 L}{\partial d_{jD} \partial d_{kF}} = \int_{\Omega_c} \alpha_c \left(N_{F,I}^{\underline{j}} S_{IJ} N_{D,J}^{\underline{j}} + F_{\underline{j}I} C_{IJKL} F_{\underline{k}K} N_{D,J}^{\underline{j}} N_{F,L}^{\underline{k}}\right) d\mathbf{X}, \\ J_{\lambda c} &= \frac{\partial^2 L}{\partial d_{jD} \partial l_{kG}} = \int_{\Omega_o} N_{G,I}^{\underline{k}} N_{D,I}^{\underline{k}} d\mathbf{X}, \\ J_d &= \frac{\partial^2 L}{\partial x_{im} \partial x_{jn}} = \sum_{m=1}^{N_m} \sum_{n=1}^{N_m} \alpha_d \mathbf{H}_{mn}, \\ J_{\lambda d} &= \frac{\partial^2 L}{\partial x_{im} \partial d_{kG}} = - \int_{\Omega_o} N_{G,I}^{\underline{k}} N_{m,I}^{\underline{k}} d\mathbf{X}, \end{aligned} \tag{44}$$

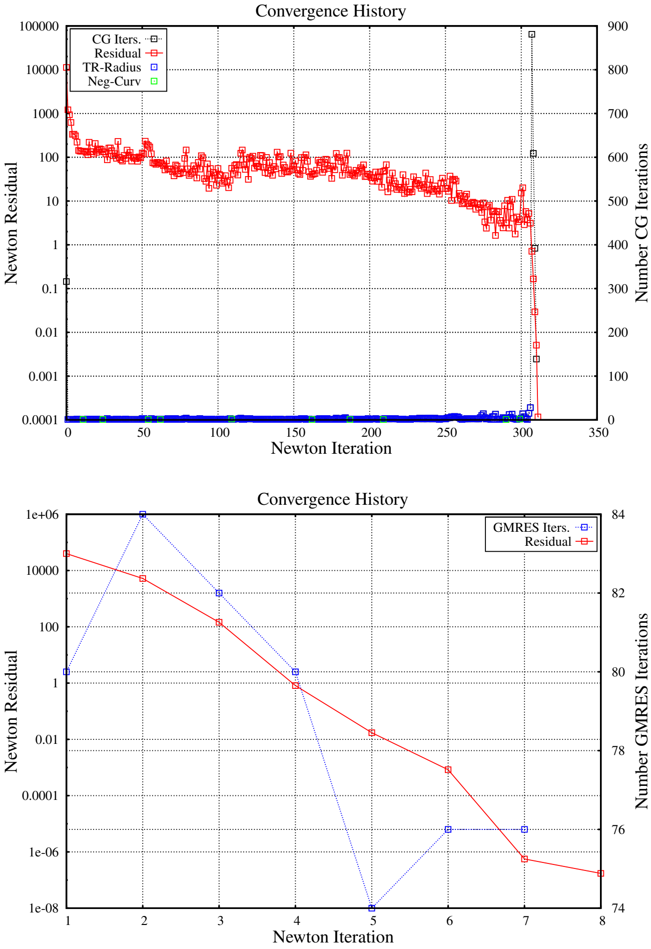

Fig. 21. Convergence behavior of a 51 × 51 × 51 and its approximation by an Arlequin model coupling the particle with a nonlinear elastic continuum. The red curve shows the value of the residual and the blue curve is this number of C–G (GMRES) iterations required at each step. (For interpretation of the references to colour in this figure legend, the reader is referred to the web version of this article.)

and $\mathbf{H}_{mn}$ correspond to intermolecular Hessians. The Hessian of the energy for a harmonic bond is

$$\mathbf{H}_{mn} = k_{mn}\left(1 - \frac{r^0_{mn}}{r_{mn}}\right)\mathbf{I} + k_{mn} r^0_{mn} \Delta\mathbf{x} \otimes \Delta\mathbf{x}. \tag{45}$$

See [6].

4.3. Numerical example

For the following numerical example, $\alpha_c = \alpha_d = 1/2$ in the overlap region Ω_o, the polymer model used corresponds to that introduced in Section 2, and the continuum model is the nonlinear elastic Mooney–Rivlin material with parameters given in Table 3. Consider the approximation of a 51 × 51 × 51 polymer lattice by an Arlequin surrogate consisting of 139 tri-linear finite elements with 17 more for Lagrange multiplers and 21 × 21 × 10 particles. This corresponds to 18,228 unknowns, compared to the 375,000 unknowns for the full polymer model: a factor of almost 21 in savings. The shrinkage parameter $\lambda = 1.3$ for this case. The convergence results for both the base model and the surrogate are shown in Fig. 21 and the equilibrium configuration of the surrogate is in Fig. 22.

The total solve time was approximately 1.4 CPU hours on 32 processors for the base model while the surrogate model converged in under 5 min on a single processor, a factor of roughly 17. Aside from the system being much smaller, the continuum part of the coupled model appears to smoothen the residual function as only 8 Newton iterations were required to attain convergence while over 300 were required for the base model. This represents a substantial performance gain.

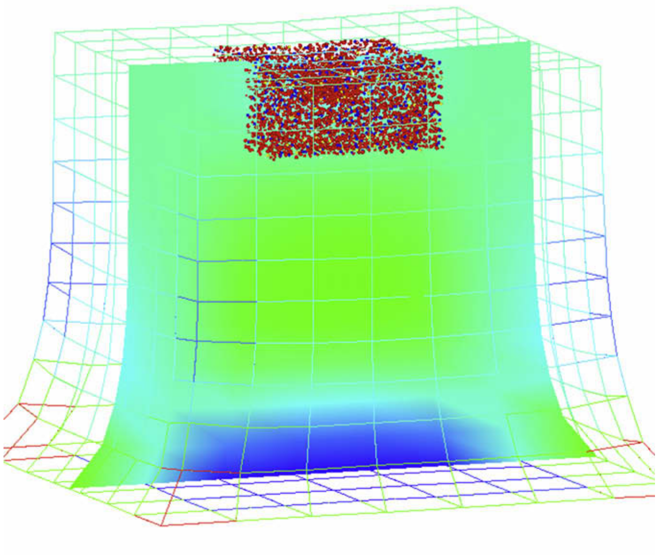

Fig. 22. Equilibrium configuration of an Arlequin approximation to a 51 × 51 × 51 polymer lattice. The mesh is colored by elements of the *zz*-component of the Cauchy stress while the slice is the interpolated *zz*-Cauchy stress. Red particles correspond to monomers, blue to crosslinkers, and yellow to initiators. (For interpretation of the references to colour in this figure legend, the reader is referred to the web version of this article.)

5. Goal-oriented error estimation and adaptivity

5.1. Adjoint problem and calculation of residual

The adjoint problem for the base model is given in (5). However, in the case of the Arlequin surrogate, the *exact* solution $\mathbf{u}$ is unknown; only the surrogate solution $\mathbf{u}_0$ is known. Thus, the primal surrogate solution exists on the space $X = V_c \times V_d$ (the displacement of particles and continuum) and V_o (the Lagrange multipliers). A projection $\Pi : X \rightarrow V$ must be used in order to compute the adjoint solution for the base model problem. In this case, the following map is used:

(i) Particle part of Arlequin model: assign the value of the displacement to the corresponding particle in the base model
(ii) Continuum part of Arlequin model:
  - Loop over all particles contained in the continuum region
  - Determine element location of particle i in finite element mesh reference configuration.
  - Obtain master element coordinates (ξ, η, ζ) by solving $\mathbf{x}^0_i - \mathbf{X}(\xi, \eta, \zeta) = 0$ in the reference configuration where $\mathbf{x}^0_i$ is the initial position of particle i.
  - Evaluate $\mathbf{u}^h(\xi, \eta, \zeta)$ and assign the value to particle i in the lattice.
(iii) Overlap part of Arlequin model: there are several choices, but the combination $\alpha_c \mathbf{u}(\mathbf{x}^0_i) + \alpha_d \mathbf{x}_i$ is taken here.

Fig. 23 illustrates the results of the above projection from an Arlequin approximation of a uniform lattice.

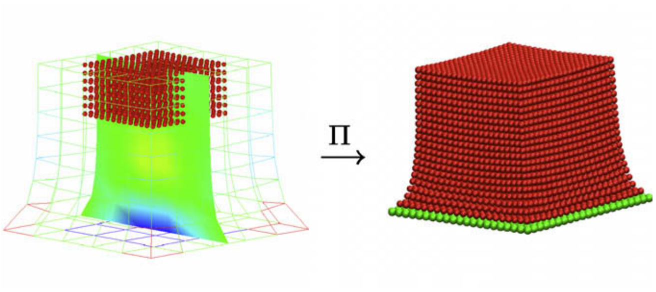

Fig. 23. The result of projection Π on an Arlequin approximation of a 21 × 21 × 21 uniform lattice. In the overlap region, the particle position is used for projecting the displacement, as opposed to the continuum.

Finally, the Lagrange multiplier is superfluous in the context of this projection and is neglected.

Thus, the following approximation to the adjoint problem is made:

$$\text{Find} \quad \hat{\mathbf{p}} \in V \text{ such that } \quad B'(\Pi\mathbf{u}_0; \mathbf{v}, \hat{\mathbf{p}}) = Q'(\Pi\mathbf{u}_0; \mathbf{v}) \quad \forall \mathbf{v} \in V, \tag{46}$$

where $\hat{\mathbf{p}}$ is the adjoint solution corresponding to the projected surrogate solution $\Pi\mathbf{u}_0$. This notation is introduced in order to differentiate this approximate adjoint solution from the exact adjoint solution $\mathbf{p}$. The only approximation made here is the use of $\Pi\mathbf{u}_0$ in place of $\mathbf{u}$.

With the calculation of the adjoint solution, the residual can be computed and errors in quantities of interest can be estimated. Recall that the error estimate is

$$\mathscr{E} = \mathscr{R}(\mathbf{u}_0; \mathbf{p}_0) + \mathscr{R}(\mathbf{u}_0; \mathbf{p} - \mathbf{p}_0) + \Delta. \tag{47}$$

In this case

$$\hat{\mathscr{E}} = \mathscr{R}(\Pi\mathbf{u}_0; \hat{\mathbf{p}}) + \mathscr{R}(\Pi\mathbf{u}_0; \mathbf{p} - \hat{\mathbf{p}}) + \Delta. \tag{48}$$

The Δ term is neglected in all examples that follow. The effect of neglecting the term $\mathscr{R}(\mathbf{u}_0; \mathbf{p} - \hat{\mathbf{p}})$ is investigated in the numerical examples.

5.2. Numerical examples: error estimation

5.2.1. Polymer lattice, continuum surrogate

Preliminary results are given here to illustrate the solution of the finite element problem and preliminary error estimation calculations. Fig. 24 shows a block under uniaxial loading in the positive x-plane and fixed in the zero x-plane.

Corresponding loading and boundary conditions are applied to a 20 × 20 × 20 realization of the polymer lattice model (post relaxation). As an example, the quantity of interest is selected to be the length of the body. In particular, the differences in the average of the x-position of the positive and zero x-faces is taken as the quantity of interest:

$$Q(\mathbf{x}) = \frac{1}{N_{x+}} \sum_{i=1}^{N_{x+}} x_i^1 - \frac{1}{N_{x-}} \sum_{i=1}^{N_{x-}} x_i^1. \tag{49}$$

Thus, the right-hand side of the adjoint problem (5) is

$$Q'(\mathbf{x}) = \begin{cases} \frac{1}{N_{x+}} & \text{if particle on } x+ \text{face}, \\ -\frac{1}{N_{x-}} & \text{if particle on } x- \text{face}, \\ 0 & \text{otherwise}, \end{cases} \tag{50}$$

There is no approximation here to the adjoint solution so that the error in the quantity of interest is given by $(8)_2$.

Results of this test of the model error estimation are as follows: exact quantity of interest: $Q(\mathbf{x}) = 78.41$; surrogate approximation: $Q(\mathbf{x}_0) = 74.65$; estimated error $Q(\mathbf{x}) - Q(\mathbf{x}_0) \approx \mathscr{R}(\Pi\mathbf{x}_0, \mathbf{p}) = 3.58$; effectivity index $\eta_{\text{eff}} = |\mathscr{R}(\mathbf{x}_0, \mathbf{p})|/|Q(\mathbf{x}) - Q(\mathbf{x}_0)| = 0.95$. The effectivity index of 0.95 establishes a quite acceptable error of only five percent in the estimated error in the quantity of interest. This result also suggests that for problems of this type, a continuum model may well be adequate for calculating such global quantities of interest.

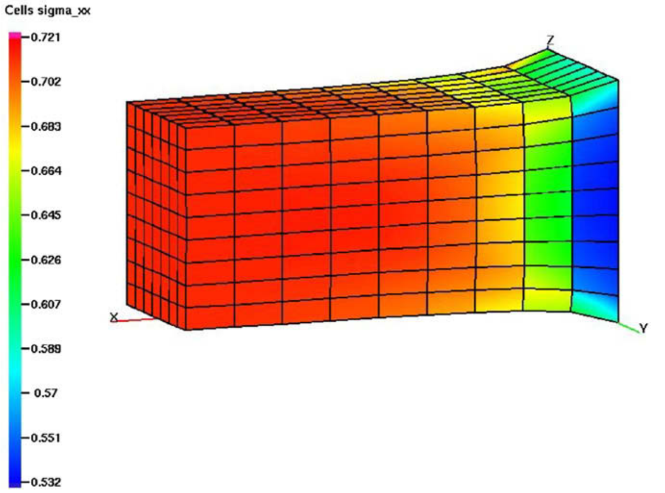

Fig. 24. A 10^3 discretization of a cube. A uniform axial load is applied on the external (free) x-face while the zero x-face is fixed in all directions. A slice is taken to show the interior stress distribution.

5.2.2. Uniform lattice, Arlequin surrogate

In this case, a 21 × 21 × 21 uniform lattice is approximated by an Arlequin surrogate model. The parameters for the bonds in the base model are $k_{ij} = 3.0$, $r_{ij}^0 = 3.0$ for axial springs and $k_{ij} = 3.0$, $r_{ij}^0 = 3.0\sqrt{2}$ for diagonal springs; the initial lattice spacing is 4.0 units. The Arlequin surrogate model consists of 174 tri-linear elements, 17 tri-linear Lagrange multiplier elements (for the overlap region), and 1183 particles. The constitutive equation for the continuum is the compressible Mooney–Rivlin material with coefficients $C_1 = 1.0, C_2 = 1.0, C_3 = 1.0$. The shrinkage parameter $\lambda = 1.33$. The quantity of interest is the "slump": the average z-displacement of a 3 × 3 patch on the positive z-face of the body. That is

$$Q(\mathbf{u}_0) = \frac{1}{|\mathscr{P}|} \sum_{i \in \mathscr{P}} u_i^z, \tag{51}$$

where $\mathscr{P}$ is the set of particles in the 3 × 3 patch and u_i^z is the z-component of the displacement of particle i. Note that we do not need to project the surrogate solution to evaluate the quantity of interest because it is defined within the particle region. Fig. 25 displays the adjoint solution and Fig. 26 the residual. Table 4 summarizes the results of the calculation. The effectivity indices η and $\hat{\eta}$ are defined as

$$\begin{aligned} \eta &= \frac{|\mathscr{R}(\Pi\mathbf{u}_0, \mathbf{p})|}{|Q(\mathbf{u}) - Q(\mathbf{u}_0)|}, \\ \hat{\eta} &= \frac{|\mathscr{R}(\Pi\mathbf{u}_0, \hat{\mathbf{p}})|}{|Q(\mathbf{u}) - Q(\mathbf{u}_0)|}. \end{aligned} \tag{52}$$

In this example, the remainder $|\Delta|$ is seen to be approximately 8% of the total error in the quantity of interest.

5.2.3. Polymer lattice, Arlequin surrogate

In this case, a 21 × 21 × 21 polymer lattice is approximated by an Arlequin surrogate model. The discretization of this surrogate model is exactly the same as was used in the previous example.

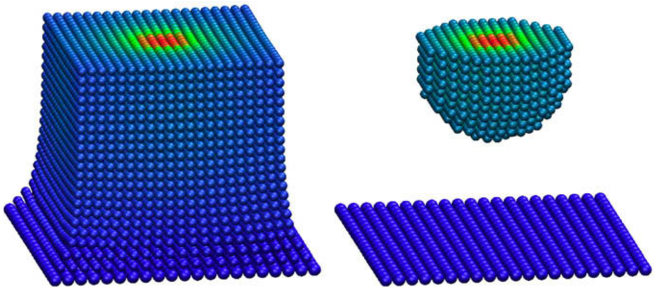

Fig. 25. (Left) the adjoint solution $\hat{p}$ corresponding to an Arlequin approximation of a 21 × 21 × 21 uniform lattice. The position of the particles is in the equilibrated current configuration. The value $\|\hat{\mathbf{p}}_i\|/\max_i \hat{\mathbf{p}}_i$ for each particle i is assigned a color in the figure, with red the highest values and blue the lowest. (Right) here, the substrate particles are shown along with particles that have $\|\hat{\mathbf{p}}_i\|/\max_i \hat{\mathbf{p}}_i > 0.3$. This represents the region that most strongly influences the value of the quantity of interest.

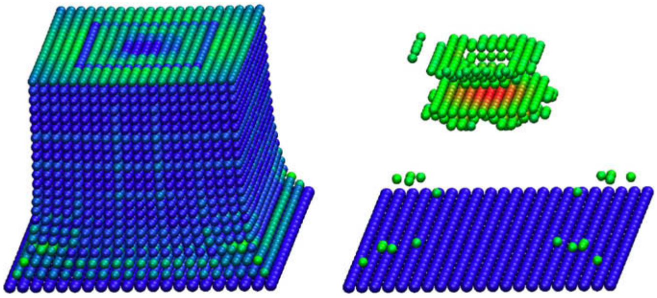

Fig. 26. (Left) the residual $\mathscr{R}(\Pi \mathbf{u}_0, \hat{\mathbf{p}})$ corresponding to an Arlequin approximation of a 21 × 21 × 21 uniform lattice. The position of the particles is in the equilibrated current configuration. The value of $\mathscr{R}_i(\Pi \mathbf{u}_0, \hat{\mathbf{p}})/\max_i \mathscr{R}_i(\Pi \mathbf{u}_0, \hat{\mathbf{p}})$, where $\mathscr{R}_i(\Pi \mathbf{u}_0, \hat{\mathbf{p}}) = (\partial E_i(\Pi \mathbf{u}_0)/\partial \mathbf{u}) \cdot \hat{\mathbf{p}}_i$, for each particle i is assigned a color in the figure, with red the highest values and blue the lowest. (Right) here, the substrate particles are shown along with particles that have $\mathscr{R}_i(\Pi \mathbf{u}_0, \hat{\mathbf{p}})/\max_i \mathscr{R}_i(\Pi \mathbf{u}_0, \hat{\mathbf{p}}) > 0.4$. This represents the region that most strongly contributes to the error in the quantity of interest. In this case, the error is primarily at the interface of the particle and continuum models, as expected.

Table 4
Results of an Arlequin approximation of a 21 × 21 × 21 uniform lattice with the quantity of interest being the average z-displacement of a 3 × 3 patch on the positive z-surface of the body.

$Q(\mathbf{u})$	$Q(\mathbf{u}_0)$	$\mathscr{R}(\Pi \mathbf{u}_0, \mathbf{p})$	$\mathscr{R}(\Pi \mathbf{u}_0, \hat{\mathbf{p}})$	η	$\hat{\eta}$
−24.5	−22.2	−2.49	−2.17	1.08	0.94

The constitutive equation for the continuum is the compressible Mooney–Rivlin material with coefficients given in Table 3. The shrinkage parameter $\lambda = 1.3$. The quantity of interest is the slump (51). Thus, this example serves to illustrate the effects of inhomogeneity in the lattice. Fig. 27 displays the (projected) adjoint solution and Fig. 28 the residual. Table 5 summarizes the results from the calculation.

The inhomogeneity has affected the quality of the error estimate by approximately 20%. This is likely due to the fact that the projection is smooth in the overlap region where the actual particle positions in the base model are much more irregular. It would seem that, for the polymer model, a more robust projection method could improve the error estimate, but this is not studied in the present work.

5.3. Adaptive algorithm

The adaptive modeling algorithm to be applied in the Goals algorithm involves first partitioning the domain into cells that will be labeled by the model used within that region. For simplicity, the partition will coincide exactly with the finite element discretization of the continuum that covers the particle model. Fig. 29 is an example of such a partition.

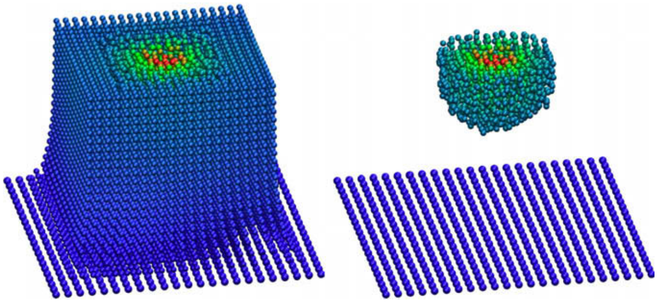

Fig. 27. Analogous results to Fig. 25 for the case of a 21 × 21 × 21 polymer lattice.

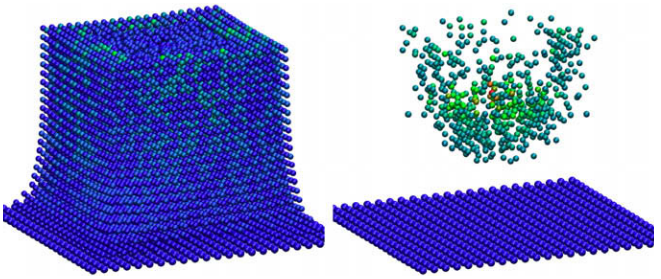

Fig. 28. Analogous results to Fig. 26 for the case of a 21 × 21 × 21 polymer lattice.

Table 5
Analogous results to Table 4 for the case of a 21 × 21 × 21 polymer lattice.

$Q(\mathbf{u})$	$Q(\mathbf{u}_0)$	$\mathscr{R}(\Pi \mathbf{u}_0, \mathbf{p})$	$\mathscr{R}(\Pi \mathbf{u}_0, \hat{\mathbf{p}})$	η	$\hat{\eta}$
−55.63	−35.0	−30.3	−14.8	1.47	0.72

Furthermore, the residual error estimate (48) must be partitioned in the same manner:

$$\mathscr{R}(\Pi \mathbf{u}_0, \hat{\mathbf{p}}) = \sum_{c=1}^{N_p} \mathscr{R}_c(\Pi \mathbf{u}_0, \hat{\mathbf{p}}), \tag{53}$$

N_p being the number of partitioned cells, c labels each cell, and $\mathscr{R}_c(\Pi \mathbf{u}_0, \hat{\mathbf{p}})$ is the value of the residual in cell c. The value of $\mathscr{R}_c(\Pi \mathbf{u}_0, \hat{\mathbf{p}})$ is computed by

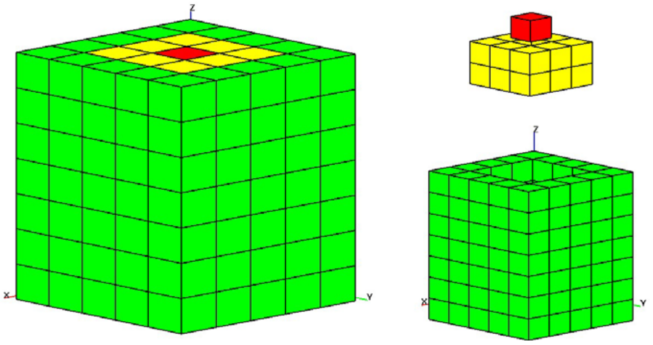

Fig. 29. The partition of the Arlequin domain. Red cells denote regions modeled using the particle model, green cells use the continuum model, and the yellow cells represent the overlap region between the two. (For interpretation of the references to colour in this figure legend, the reader is referred to the web version of this article.)

$$\mathscr{R}_c(\Pi\mathbf{u}_0,\hat{\mathbf{p}}) = \sum_{i\in c}\sum_{j=1}^{n_i} \frac{\partial E_{ij}(\Pi\mathbf{u}_0)}{\partial \mathbf{u}_i}\cdot\hat{\mathbf{p}}_i. \tag{54}$$

Note that if the particle i is on a boundary between cells, it is scaled by the number of cells it overlaps. For instance, if a particle is on a face and belongs to two cells it is scaled by 1/2. Fig. 30 shows an example of the distribution of error.

Thus, the adaptive algorithm proceeds as follows.

(i) Specify the error tolerance for the quantity of interest, γ_{tol} and the refinement parameter α_a.
(ii) Solve the primal surrogate problem (4).
(iii) Compute the projection $\Pi\mathbf{u}_0$ of surrogate problem. Solve the adjoint problem (46).
(iv) Compute the residual (48). If $\mathscr{R}(\Pi\mathbf{u}_0,\hat{\mathbf{p}})/Q(\mathbf{u}_0) < \gamma_{\text{tol}}$, then stop. Otherwise, goto step (v).
(v) Partition the residual: compute $\mathscr{R}_c(\Pi\mathbf{u}_0,\hat{\mathbf{p}})$ for each cell c.
(vi) Relabel cells as "particle" cells if: $\mathscr{R}_c(\Pi\mathbf{u}_0,\hat{\mathbf{p}}) > \alpha_a\max_c\mathscr{R}_c(\Pi\mathbf{u}_0,\hat{\mathbf{p}})$. That is, if a cell c has a residual a fraction α_a of the maximum, then that cell is "refined" and relabeled as particle, i.e. the particle structure is supplied to this cell.
(vii) Reconfigure overlap region to be consistent with new particle configuration.
(viii) Goto step (ii).

5.4. Numerical examples: adaptivity

The same data are used here as the example on error estimation. The adaptivity parameters are taken to be $\alpha_a = 0.4$ and $\gamma_{\text{tol}} = 0.05$. Table 6 lists the error and effectivity indices computed during the five adaptive steps for the uniform case while Table 7 lists these quantities for the polymer case. The quantity $\mathscr{E}_r$ is defined by

$$\mathscr{E}_r = \frac{\mathscr{R}(\Pi\mathbf{u}_0,\hat{\mathbf{p}})}{Q(\mathbf{u}_0)}. \tag{55}$$

Figs. 31 and 32 show the configurations chosen by the adaptive algorithm and Fig. 33 shows the partition of the residual for each configuration for the uniform lattice and Figs. 34–36 depict the same information for the polymer case.

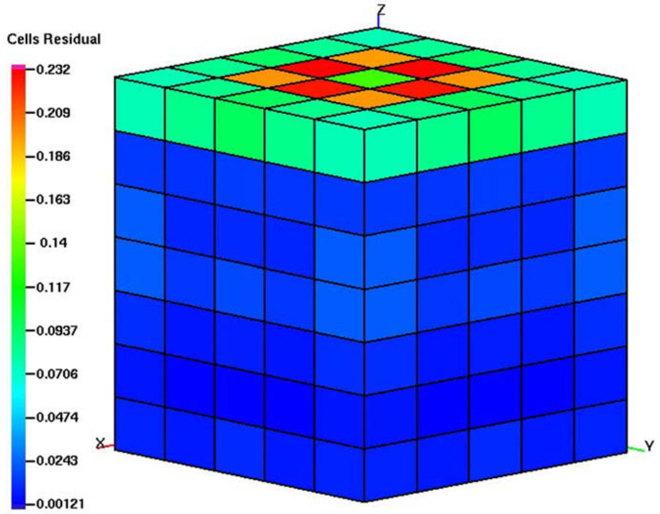

Fig. 30. The residual partitioned over the domain.

Table 6
Results of the Goals algorithm for a 21 × 21 × 21 uniform lattice with an Arlequin surrogate model. A total of five adaptive steps were needed to bring the error in the quantity of interest to within 5%.

Adaptive step	$\mathscr{E}_r$ (%)	η	$\hat{\eta}$
0	9.77	1.08	0.94
1	8.24	1.09	0.93
2	7.71	1.10	0.93
3	6.75	1.11	0.92
4	5.08	1.16	0.88
5	4.74	1.10	0.92

Table 7
Results of the Goals algorithm for a 21 × 21 × 21 polymer lattice with an Arlequin surrogate model. A total of five adaptive steps were needed to bring the error in the quantity of interest to within 6%.

Adaptive step	$\mathscr{E}_r$ (%)	η	$\hat{\eta}$
0	42.2	1.47	0.71
1	30.8	1.41	0.67
2	18.6	1.52	0.59
3	13.5	1.56	0.51
4	10.2	1.45	0.48
5	5.34	1.37	0.36

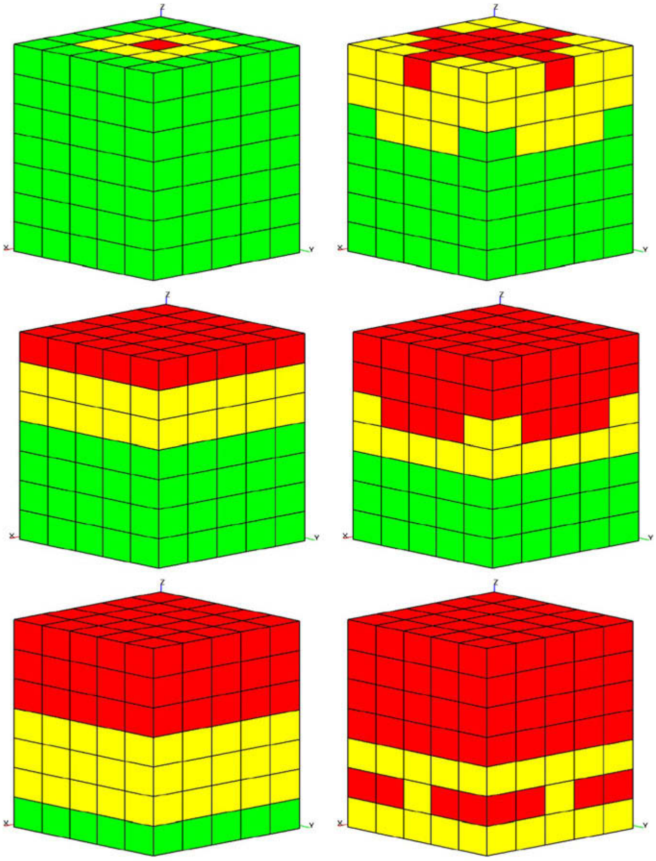

Fig. 31. The configurations chosen by the adaptive algorithm for a 21 × 21 × 21 uniform lattice with an Arlequin surrogate model and $\alpha_a = 0.4$ and $\gamma_{\text{tol}} = 0.05$. Red cells denote particle model regions, green cells the continuum model, and yellow cells denote the overlap regions. (For interpretation of the references to colour in this figure legend, the reader is referred to the web version of this article.)

6. Approximation of adjoint solution and residual calculation

In the previous section, strategies to project the Arlequin solution onto the full lattice space, solve the adjoint problem, and compute

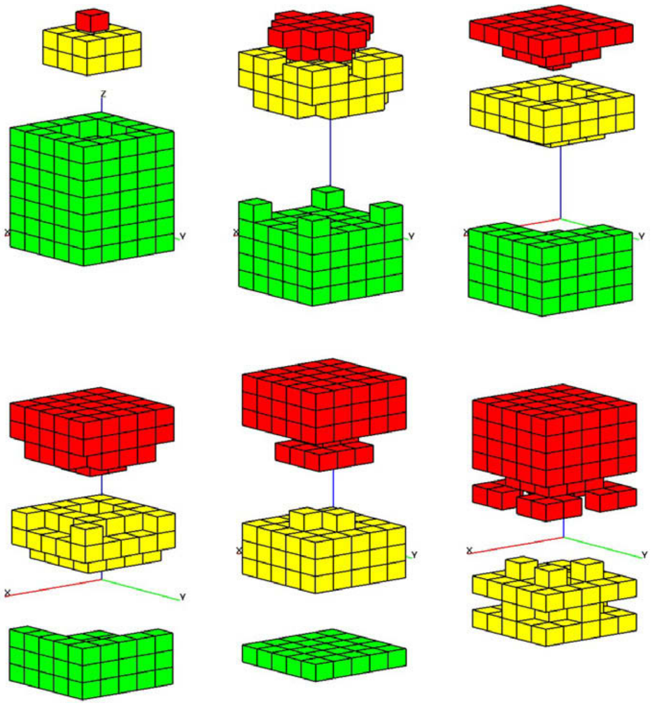

Fig. 32. Exploded view of the configurations chosen by the adaptive algorithm for a $21 \times 21 \times 21$ uniform lattice with an Arlequin surrogate model and $\alpha_a = 0.4$ and $\gamma_{\text{tol}} = 0.05$.

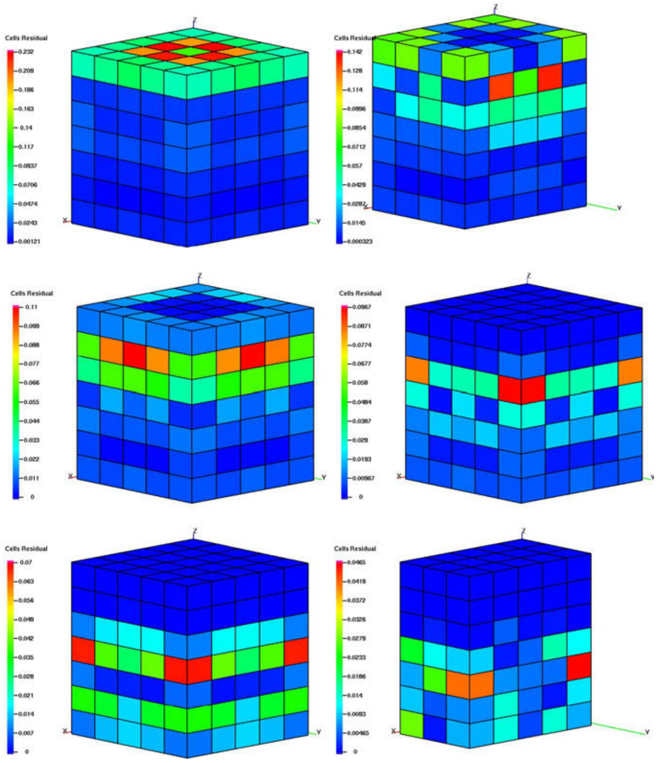

Fig. 33. The residual partition for each step of the adaptive algorithm for a $21 \times 21 \times 21$ uniform lattice with an Arlequin surrogate model and $\alpha_a = 0.4$ and $\gamma_{\text{tol}} = 0.05$. In some cases, the image is sliced to expose regions containing the greatest amount of error.

the residual were discussed in detail. Furthermore, an adaptive algorithm was introduced. However, in practical applications, alternative techniques should be considered to compute both the adjoint and residual for error estimation as the systems of practical interest would become too large to be modeled by the full lattice. Examples of such strategies are discussed in the present section.

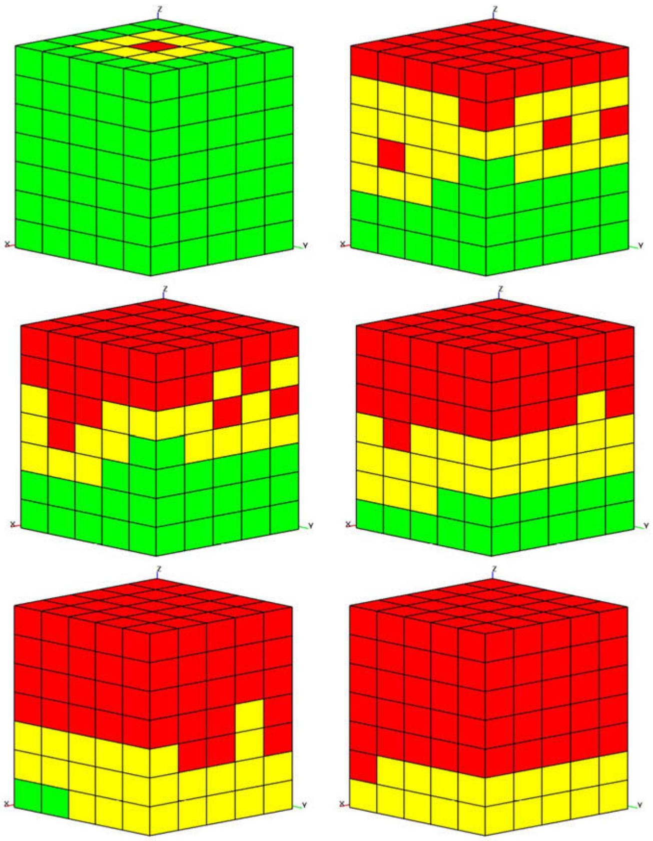

Fig. 34. The configurations chosen by the adaptive algorithm for a $21 \times 21 \times 21$ polymer lattice with an Arlequin surrogate model and $\alpha_a = 0.4$ and $\gamma_{\text{tol}} = 0.06$.

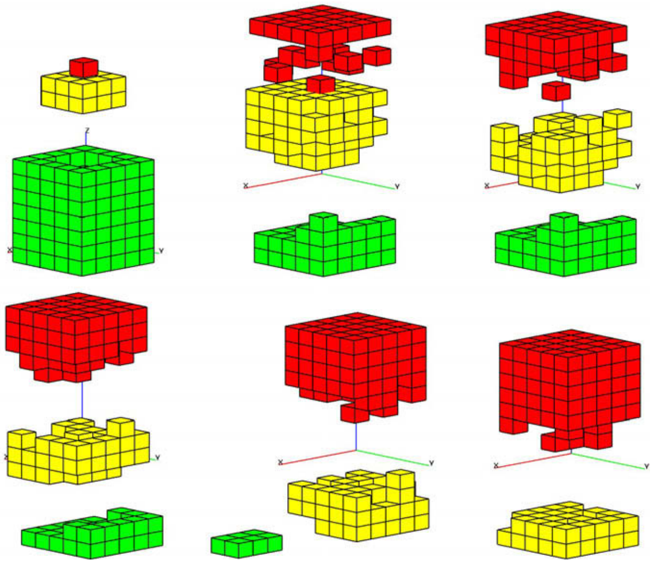

Fig. 35. Exploded view of the configurations chosen by the adaptive algorithm for a $21 \times 21 \times 21$ polymer lattice with an Arlequin surrogate model and $\alpha_a = 0.4$ and $\gamma_{\text{tol}} = 0.06$.

6.1. Adjoint and residual approximations

Recall that in order to compute error estimates in quantities of interest using the Arlequin surrogate solutions, a projection

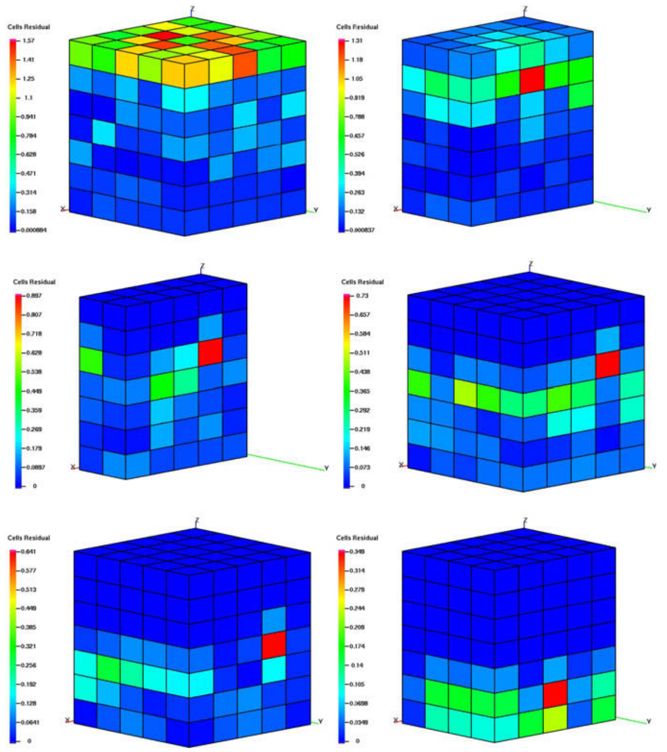

Fig. 36. The residual partition for each step of the adaptive algorithm for a $21 \times 21 \times 21$ polymer lattice with an Arlequin surrogate model and $\alpha_a = 0.4$ and $\gamma_{\text{tol}} = 0.05$. In some cases, the image is sliced to expose regions containing the greatest amount of error.

operator Π was introduced that mapped the mixed particle–continuum model to the full particle space. However, for applications of engineering interest, the cost of computing the adjoint solution and evaluating the residual is prohibitive. Furthermore, it is ineffective to compute the adjoint and residual with the same surrogate model since:

$$B_0(\mathbf{u}_0; \mathbf{v}_0) = F_0(\mathbf{v}_0) \quad \forall \mathbf{v}_0 \in V_0, \tag{56}$$

so that

$$\mathscr{R}_0(\mathbf{u}_0; \mathbf{p}_0) = F_0(\mathbf{p}_0) - B_0(\mathbf{u}_0; \mathbf{p}_0) = 0. \tag{57}$$

Thus, the calculation of the adjoint and residual must involve more information than that which exists in the surrogate model, while still being cost efficient.

The strategy proposed here is to enrich the surrogate model by enlarging the region of the base model *only for the calculation of the adjoint and residual*. This strategy is analogous to the one used in [28]; see also [1]. In the case of the Arlequin method, this simply means relabeling neighboring cells as particle regions. The parameter in this algorithm is the number of layers to enrich the model. A one-layer enrichment corresponds to relabeling all cells as particle regions that directly neighbor the current particle regions. Two layers would transform the nearest neighbors *and* the next nearest neighbors. Fig. 37 illustrates the idea of enrichment.

Once cells have been reconfigured, a projection must be applied so that the surrogate solution is in the correct space. This projection is denoted $\tilde{\Pi} : (X, M) \to (\tilde{X}, \tilde{M})$ and is discussed subsequently. First, the surrogate solution corresponding to continuum or particle cells that were unchanged by the enrichment procedure are left unchanged; in other words, the value of the displacements are copied to the new vector. Continuum cells that were converted to particle or overlapping cells require the addition of particles: this is accomplished using the procedure discussed in Section 5.1. The caveat here is that, unlike the case of the projection Π, the Lagrange multiplier cannot be ignored. Indeed, Fig. 37 illustrates that this procedure will *always* change the overlap region where the Lagrange multiplier is defined.

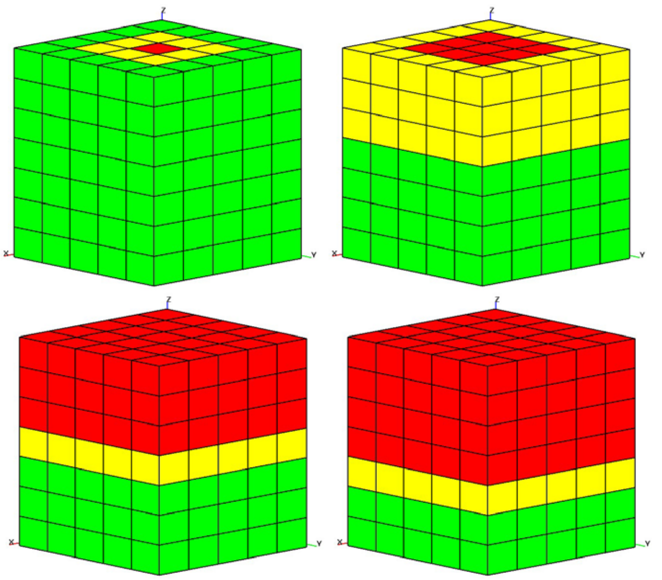

Fig. 37. Illustration of the enrichment procedure used to approximate the calculation of the adjoint solution and the evaluation of the residual. A sequence of one, two, and three layer enrichments are shown here. Red cells denote particle model regions, green cells the continuum model, and yellow cells denote the overlap regions. (For interpretation of the references to colour in this figure legend, the reader is referred to the web version of this article.)

To understand the consequences of choosing this projection on the calculation of the error estimate, the one-dimensional problem is examined. In this case

$$\begin{aligned} \tilde{V}_c &= \left\{ v \in H^1(\tilde{\Omega}_c) : v(0) = 0 \right\}, \\ \tilde{V}_d &= \left\{ z \in \mathbb{R}^{\tilde{m}+1} \right\}, \\ \tilde{X} &= \tilde{V}_c \times \tilde{V}_d, \end{aligned} \tag{58}$$

and

$$\tilde{M} = \begin{cases} H^1(\tilde{\Omega}_o)/\mathbb{R}, & \text{if } \beta_1 = 0, \\ H^1(\tilde{\Omega}_o), & \text{otherwise}, \end{cases} \tag{59}$$

where the $(\tilde{\cdot})$ symbols correspond to the enriched configuration. Then, the (enriched) adjoint problem is

$$\begin{aligned} &\text{Find} \quad \tilde{P} \in \tilde{X}, \tilde{p}_\lambda \in \tilde{M} \text{ such that :} \\ &\tilde{a}(\tilde{V}, \tilde{P}) + b(\tilde{p}_\lambda, \tilde{V}) = Q(\tilde{V}) \quad \forall \tilde{V} \in \tilde{X} \\ &b(\tilde{\mu}, \tilde{P}) = 0 \quad \forall \tilde{\mu} \in \tilde{M}, \end{aligned} \tag{60}$$

where $\tilde{P} = (\tilde{p}_c, \tilde{p}_d)$ and $\tilde{p}_c$, $\tilde{p}_d$, $\tilde{p}_\lambda$ are the continuum, discrete, and Lagrange multiplier components of the adjoint solution. Thus, it is clear that the adjoint solution satisfies the constraint on the overlap region. In particular, letting $\tilde{\Pi}\lambda$ correspond to the (at this point, arbitrary) choice of the projection of the Lagrange multiplier,

$$\begin{aligned} \tilde{\mathscr{R}}(\tilde{\Pi}U, \tilde{P}) &= \tilde{a}(\tilde{\Pi}U, \tilde{P}) + b(\tilde{\Pi}\lambda, \tilde{P}) + b(\tilde{p}_\lambda, \tilde{U}) \\ &= \tilde{a}(\tilde{\Pi}U, \tilde{P}) + b(\tilde{p}_\lambda, \tilde{\Pi}U), \end{aligned} \tag{61}$$

since $b(\tilde{\mu}, \tilde{P}) = 0 \forall \tilde{\mu} \in \tilde{M}$. Thus, the choice of $\tilde{\Pi}\lambda$ has no effect on the calculation of the error estimate for the quantity of interest.

Although the constraint is strongly enforced in the continuous case, the constraint is only weakly enforced in the discrete case. Therefore, the constraint will not necessarily be enforced element-wise. The implication here is on the adaptive algorithm.

Table 8
Effectivity indices for various levels of enrichment using the approximate adjoint, and then both approximate residual and adjoint on a 21 × 21 × 21 uniform lattice with an Arlequin surrogate. The indices computed using the exact dual and residual are inserted for comparison.

η	$\hat{\eta}$	Enrichment level	$\tilde{\eta}$	$\tilde{\tilde{\eta}}$
1.08	0.94	5	0.69	0.74
		4	0.58	0.57
		3	0.53	0.37
		2	0.45	0.26
		1	0.36	0.15

Table 9
Analogous results to Table 8 for the case of a 21 × 21 × 21 polymer lattice.

η	$\hat{\eta}$	Enrichment level	$\tilde{\eta}$	$\tilde{\tilde{\eta}}$
1.47	0.72	5	0.64	0.67
		4	0.59	0.57
		3	0.48	0.43
		2	0.39	0.32
		1	0.23	0.16

When the residual is partitioned over the domain, although the effects of the term $b(\tilde{\lambda}, \tilde{P})$ will cancel when the residual partition is summed, it will locally pollute the residual value. For the numerical results presented, the local pollution is on the order of 1–5% of the value of the cell residual $\mathscr{R}_c(\tilde{\Pi}\mathbf{u}_0, \tilde{\mathbf{p}})$. This effect is considered to be small and is neglected.

6.2. Numerical results

We repeat the numerical experiments of Section 5.2. In addition to the previously defined effectivity indices, we also introduce

$$\tilde{\eta} = \frac{|\mathscr{R}(\Pi\mathbf{u}_0, \Pi\tilde{\mathbf{p}})|}{|Q(\mathbf{u}) - Q(\Pi\mathbf{u}_0)|}, \qquad \tilde{\tilde{\eta}} = \frac{\left|\tilde{\mathscr{R}}(\tilde{\Pi}\mathbf{u}_0, \tilde{\mathbf{p}})\right|}{\left|Q(\mathbf{u}) - Q(\tilde{\Pi}\mathbf{u}_0)\right|}. \tag{62}$$

The quantity $\tilde{\eta}$ represents the effectivity index for the case when the adjoint solution is computed on the enriched configuration, but is then projected to the full lattice (along with $\mathbf{u}_0$) and the full lattice residual evaluated. Similarly, the term $\tilde{\tilde{\eta}}$ is for the case when the adjoint computed on the enriched configuration and the residual corresponding to the enriched Arlequin configuration is evaluated. Table 8 shows the effectivity indices for various levels of enrichment for the uniform case while Table 9 shows the same results for the polymer case. Note that in both cases, enrichments greater than five levels will lead to dual and residual calculations on the full lattice space.

As the results show, the fidelity of the error estimate can be severely compromised depending on the enrichment level used for the error estimate. This is particularly true in the uniform case. In the polymer case, even the moderate level of enrichments yield error estimates within 15% of the error estimates without approximating the dual or residual. This may be due to the fact that the quantity of interest is more global in nature and that more local quantities will yield better results. This requires further investigation.

7. Summary and conclusions

Our goal in this work was to present computational methods for multiscale modeling of molecular systems employing both particle–continuum coupling techniques and error estimation and adaptive modeling algorithms in order to control modeling error in quantities of interest. This entailed the specification of a base model of molecular statics of polymers, the coarse graining of the particle model to a nonlinear elastic continuum model, the coupling of the two via the Arlequin method, estimating the error incurred by using such surrogate models, and adapting the model to control the error in specific quantities of interest.

The base model is chosen to be a lattice model of polymers where the polymer network is constructed using a Monte-Carlo type algorithm that models the chemical kinetics of the material. Harmonic potentials are assigned to bonds that are formed during this process. A molecular statics problem is posed on the resulting lattice of molecules. It is observed that not only is the immense size of realistic simulations a limiting factor of the model, but also is the challenge of efficiently finding a solution. Indeed, as the problem size grows, also does the number of Newton iterations.

Based on arguments from statistical mechanics, as well as experimental evidence, a nonlinear elastic continuum model is chosen as a coarse grain representation of the base model. Numerical experiments on representative volume elements (RVE's) are used to determine coefficients for the continuum model so that it is as compatible as possible with the underlying particle model. Furthermore, a simple augmentation to the classical finite element approximation is introduced to account for the inherent initial strain present in the molecular model.

With the particle and continuum models properly defined, the next step is to couple the two to construct the surrogate model used to approximate the base model. The coupling here is based on the Arlequin method where Lagrange mulipliers enforce constraints on the displacements and derivatives on a region of overlap between the particle and continuum model. This surrogate is implemented in a three-dimensional setting where the base polymer model is coupled to the nonlinear elastic continuum model developed previously. It is shown that use of the surrogate model provides a substantial cost benefit in both computer resources required as well as simulation time. This is due not only to the smaller size of systems being solved, but also to the smoothing of the energy landscape of the particle model by use of the continuum model in appropriate subdomains.

Finally, the Goals framework is implemented employing the Arlequin surrogate that is constructed. Error estimates are computed for several numerical examples where the adjoint and residual are computed exactly, as well as the case where the surrogate primal solution is used in the solution of the adjoint problem. For uniform lattices, the results are very good with effectivity indices on the order of $0.92 - 1.08$. While the results are still acceptable for the polymer case, the effectivity indices are in the range 0.72–1.4. The error estimates are then used to drive an adaptive algorithm where the residual is partitioned over the domain and the cells are selected for refinement, i.e. the model becomes the particle model in the cells where the contributions to the error are the largest. It is seen that the adaptive algorithm controls the error to within the specified tolerance although the refinement procedure can require many refinements. This indicates that either the quantity of interest is global in nature or the models are incompatible.

The same adaptive procedure was also implemented with error estimates computed with approximate adjoint solutions and residual calculations. This idea is based on enriching the current model partition to include more of the base model features just for the calculation of the adjoint and residual so as to have enough information to obtain a reasonable error estimate, but at a much lower cost than the cost of computing the full adjoint and residual. As expected, for low enrichment, the effectivity indices suffer, but as the model is enriched further, the estimates of the error became comparable to those obtained with the exact dual and residual calculations. This is especially true in the case of the polymer model.

The results presented here demonstrate that *a posteriori* estimates of relative modeling error can provide an effective basis for model adaptivity as well as a basis for decision making on the influence of features of various scales on specific quantities of interest. Importantly, we feel that these approaches may prove to be very useful in designing and optimizing nano-manufacturing processes employed in imprint lithography.

Although the current work represents a major step in an effort towards the development of an accurate and robust methodology, there remains much work to be done. Key to the framework discussed here is the validity of the base model. The subject of validation is receiving a great deal of attention at present and we hope to present progress on the development of statistical methods of validation of the base model in future work. Furthermore, the base model presented in this work is a stochastic one, but only specific realizations have been considered heretofore. The incorporation of stochastic methods to the proposed numerical methods is under investigation [14,15].

Acknowledgements

The authors wish to thank Dr. C. Grant Willson, Dr. Leszek Demkowicz, Dr. Jon Bass, Dr. Greg Rodin, Dr. Peter Rossky, Elizabeth Collister, and Chetan Jhurani for their many helpful discussions in our weekly meetings over the three-year period of this work. Serge Prudhomme is also very grateful to H. Ben Dhia of the Laboratoire de Mécanique des Sols, Structures et Matériaux (LMSSMAT) for the many fruitful discussions during his stay at Ecole Centrale de Paris in May–June 2006 and June 2007 and preliminary collaborative work on the subject. Paul T. Bauman was supported by a Department of Energy Computational Science Graduate Fellowship. J. Tinsley Oden and Serge Prudhomme were supported by DOE Grant DE-FG02-05ER25701. This support is gratefully acknowledged.

References

[1] M. Arndt, M. Luskin, Goal-oriented adaptive mesh refinement for the quasicontinuum approximation of a Frenkel–Kontorova model, Comput. Methods Appl. Mech. Engrg. 197 (2008) 4298–4306.

[2] T. Bailey, S. Johnson, D. Resnick, S. Sreenivasan, J. Ekerdt, C. Willson, Step and flash imprint lithography: an efficient nanoscale printing technology, J. Photopolym. Sci. Technol. 15 (9) (2002) 481.

[3] S. Balay, K. Buschelman, V. Eijkhout, W.D. Gropp, D. Kaushik, M.G. Knepley, L.C. McInnes, B.F. Smith, H. Zhang, PETSc users manual, Technical Report ANL-95/11 – Revision 2.1.5, Argonne National Laboratory, 2004.

[4] S. Balay, K. Buschelman, W.D. Gropp, D. Kaushik, M.G. Knepley, L.C. McInnes, B.F. Smith, H. Zhang, PETSc Web page, 2001, <http://www.mcs.anl.gov/petsc>.

[5] S. Balay, W.D. Gropp, L.C. McInnes, B.F. Smith, Efficient management of parallelism in object oriented numerical software libraries, in: E. Arge, A.M. Bruaset, H.P. Langtangen (Eds.), Modern Software Tools in Scientific Computing, Birkhäuser Press, 1997.

[6] P.T. Bauman, Adaptive multiscale modeling of polymeric materials using Goal-oriented error estimation, Arlequin coupling, and Goals algorithms, Ph.D. Thesis, The University of Texas at Austin, 2008.

[7] P.T. Bauman, H. Ben Dhia, N. Elkhodja, J.T. Oden, S. Prudhomme, On the application of the Arlequin method to the coupling of particle and continuum models, Comput. Mech. 42 (2008) 511–530.

[8] H. Ben Dhia, Multiscale mechanical problems: the Arlequin method, C. R. Acad. Sci. Ser. IIB 326 (12) (1998) 899–904.

[9] H. Ben Dhia, Global local approaches: the Arlequin framework, Eur. J. Comput. Mech. 15 (1–3) (2006) 67–80.

[10] H. Ben Dhia, G. Rateau, Application of the Arlequin method to some structures with defects, Rev. Eur. Elém. Finis 332 (2002) 649–654.

[11] H. Ben Dhia, G. Rateau, The Arlequin method as a flexible engineering design tool, Int. J. Numer. Methods Engrg. 62 (11) (2005) 1442–1462.

[12] S. Benson, L.C. McInnes, J. Moré, T. Munson, J. Sarich, TAO user manual (revision 1.9), Technical Report ANL/MCS-TM-242, Mathematics and Computer Science Division, Argonne National Laboratory, 2007, <http://www.mcs.anl.gov/tao>.

[13] R.L. Burns, S.C. Johnson, G.M. Schmid, E.K. Kim, M.D. Dickey, J. Meiring, S.D. Burns, N.A. Stacey, C.G. Willson, Mesoscale modeling for sfil simulating polymerization kinetics and densification, Proc. SPIE 5374 (2004) 348–360.

[14] L. Chamoin, J.T. Oden, S. Prudhomme, A stochastic coupling method for atomic-to-continuum Monte-Carlo simulations, Comput. Methods Appl. Mech. Engrg. 197 (2008) 3530–3546.

[15] L. Chamoin, S. Prudhomme, J.T. Oden, On coupling atomic and continuum models with random data by a stochastic collocation method, in preparation.

[16] P.G. Ciarlet, Mathematical Elasticity Volume I: Three Dimensional Elasticity, Elsevier, The Netherlands, 1988.

[17] E. Collister, Private Communication, 2008.

[18] W.A. Curtin, R.E. Miller, Atomistic/continuum coupling in computational materials science, Model. Simulat. Mater. Sci. Engrg. 11 (2003) R33–R68.

[19] M.D. Dickey, C.G. Willson, Kinetic parameters for step and flash imprint lithography photopolymerization, AIChE J. 52 (2) (2006) 777–784.

[20] W. E, X. Li, E. Vanden-Eijnden, Some recent progress in multiscale modeling, Lect. Notes Comput. Sci. Engrg. 39 (2004) 3–22.

[21] W. Humphrey, A. Dalke, K. Schulten, VMD – visual molecular dynamics, Journal of Molecular Graphics 14 (1996) 33–38. http://www.ks.uiuc.edu/Research/vmd/.

[22] W.K. Liu, E.G. Karpov, S. Zhang, H.S. Park, An introduction to computational nanomechanics and materials, Comput. Methods Appl. Mech. Engrg. 193 (2004) 1529–1578.

[23] B.K. Long, B.K. Keitz, C.G. Willson, Materials for step and flash imprint lithography, J. Mater. Chem. 17 (2007) 3575–3580.

[24] R.E. Miller, E.B. Tadmor, The quasicontinuum method: overview, applications, and current directions, J. Comput.-Aided Des. 9 (2002) 203–239.

[25] J.T. Oden, S. Prudhomme, Estimation of modeling error in computational mechanics, J. Comput. Phys. 182 (2002) 496–515.

[26] J.T. Oden, S. Prudhomme, A. Romkes, P.T. Bauman, Multi-scale modeling of physical phenomena: adaptive control of models, SIAM J. Sci. Comput. 28 (2006) 2359–2389.

[27] J.T. Oden, K. Vemaganti, Estimation of local modeling error and Goal-oriented modeling of heterogeneous materials 1. Error estimates and adaptive algorithms, J. Comput. Phys. 164 (2000) 22–47.

[28] S. Prudhomme, P.T. Bauman, J.T. Oden, Error control for molecular statics problems, Int. J. Multiscale Comp. Engrg. 4 (2006) 647–662.

[29] D. Resnick, G. Schmid, M. Miller, G. Doyle, C. Jones, D. LaBrake, Step and flash imprint lithography fabrication for emerging market applications, in: Photomask Japan, 2007, Available from: <http://www.molecularimprints.com/NewsEvents/techarticles.html>.

[30] D. Resnick, S. Sreenivasan, C.G. Willson, Step and flash imprint lithography, Mater. Today February (2005) 34–42.

[31] R.S. Rivlin, D.W. Saunders, Large elastic deformations of isotropic materials: VII experiments on the deformation of rubber, Phil. Trans. Roy. Soc. Lon. A 243 (1951) 251–288.

[32] L.R.G. Treloar, The Physics of Rubber Elasticity, Clarendon Press, Oxford, 1975.

[33] K. Vemaganti, J.T. Oden, Estimation of local modeling error and Goal-oriented modeling of heterogeneous materials; Part II: a computational environment for adaptive modeling of heterogeneous elastic solids, Comput. Methods Appl. Mech. Engrg. 190 (2001) 6089–6124.